energy&fuels

pubs.acs.org/EF
Article

Ammonia in Dual-Fueled Internal Combustion Engines: Impact on NO_x, N_2O, and Soot Formation

Krister A. Pedersen,* Michał T. Lewandowski, Corinna Schulze-Netzer, Michał Pasternak, and Terese Løvås

Cite This: https://doi.org/10.1021/acs.energyfuels.3c02549
Read Online

ABSTRACT: The combustion of ammonia in internal combustion engines (ICE) releases nitrogen-related exhaust emissions. Numerous studies have shown that the increased formation of nitrous oxide (N_2O) may offset ammonia's carbon-free advantages, leading to a higher greenhouse gas potential than fossil fuels. Moreover, nitrogen contained in ammonia further promotes an increase in NO_x formation. This study aims to expand the understanding of emission formation in dual-fuel ICEs when using ammonia as a fuel. By constant-pressure reactor simulations coupled with detailed reaction kinetics, the concept of equivalence ratio−temperature diagrams was employed to characterize conditions featuring high NO_x, N_2O, and soot concentrations. The diagrams were obtained for pure ammonia, pure *n*-heptane, and three blends with ammonia energy shares (AES) of 20, 50, and 80%. Our findings strengthen the perception that high concentrations of N_2O in ICEs are related to incomplete combustion. A higher AES leads to increased N_2O concentration during the ignition, going from single-digit ppm levels for pure *n*-heptane to conditions featuring levels 3 orders of magnitude higher for pure ammonia. In fully burned mixtures, N_2O emissions feature a low fuel dependency and single-digit concentration levels only at low equivalence ratios and high temperatures. Further, varying contributions from the fuel NO, prompt NO, and thermal De-NO_x mechanisms were observed with fuel composition; however, the thermal NO contribution led to a fuel-independent behavior for NO_x emissions at temperatures above 2600 K. The soot concentration decreases as the carbon content in the fuel decreases. In our configuration, the lowest equivalence ratio at which the 0.1% soot yield limit was observed was 2.20 for pure *n*-heptane, 2.65 for AES of 20%, 5.05 for 50% AES, and not attained for higher AES. Ultimately, it was found that in fuel-rich regimes and at fully burned conditions, low concentrations of NO_x and N_2O emissions are observed.

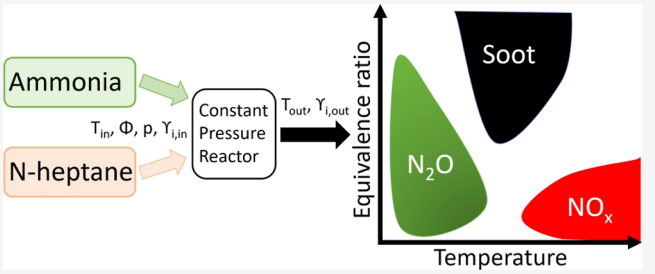

1. INTRODUCTION

Since the industrial revolution, burning fossil fuels has contributed to a continuously increasing amount of greenhouse gases (GHG) in the atmosphere. Despite the reduction in carbon dioxide (CO_2) emissions due to the Covid-19 pandemic, the highest ever average annual concentration in the atmosphere was recorded with 412.5 ppm in 2020;[1] a CO_2 concentration around 50% higher than at the start of the industrial revolution. The transport sector is a significant contributor and accounted for 27% of the total GHG emissions in 2019.[2] Decarbonizing the transport sector relies heavily upon technology development and implementation of carbon-free fuels such as hydrogen and ammonia or electrification. The challenge with electrification is the low energy densities in batteries, making them less suitable for heavy-duty long-distance transport.[3] For such applications, energy stored in chemical compounds has shown to be a promising solution.[4] Hydrogen is an energy carrier that can be either used directly as fuel or converted to electricity through fuel cells. Despite the favorable properties of hydrogen, such as H_2O as the combustion product and wide flammability limits, strict requirements for liquid storage result in high costs and relatively low overall energy efficiency.[5,6] To ease the storage requirements, hydrogen can be stored through a hydrogen carrier such as ammonia. Ammonia is easier to liquefy, making long-time energy storage and transport feasible at lower costs. It also has the advantage of a higher volumetric energy density.

Studying ammonia for internal combustion engines (ICE) dates back to the Second World War. Due to ammonia's combustion characteristics regarding low flame propagation speeds and high autoignition temperature, compression ratios up to 35 are necessary to utilize ammonia as a single fuel in compression ignition (CI) engines.[7] To facilitate the use of lower compression ratios, introducing a secondary fuel as a pilot

Received: July 12, 2023
Revised: October 6, 2023
Accepted: October 11, 2023
Published: October 27, 2023

fuel or in a dual-fuel operating technology is a viable solution.[8,9] By replacing portions of the hydrocarbon fuel with ammonia, CO_2 emissions decrease. However, ammonia could produce higher NO_x emissions due to fuel-bounded nitrogen, and increased emissions of the climate-deteriorating gas nitrous oxide (N_2O) could offset the GHG benefits.[10] N_2O is regarded as the third most important and influential long-lived greenhouse gas, behind CO_2 and methane (CH_4).[11] Its lifetime in the atmosphere and troposphere is roughly 100 years,[12] and it is a strong infrared absorber. This results in heat-trapping capabilities in the atmosphere, around 300 times stronger than CO_2. An additional consequence of N_2O pollution is that N_2O consumes ozone (O_3) to form NO, enhancing ozone depletion in the stratosphere.[11] Considering N_2O is thus crucial in optimizing engine operation. Studies have shown that the formation of N_2O in ammonia combustion is due to the two main reaction pathways, $NH_2 + NO_2 \rightleftharpoons N_2O + H_2O$ and $NH + NO \rightleftharpoons N_2O + H$, where the first pathway is the main contributor at low temperatures and the second at higher temperatures.[13] The formed N_2O by the second pathway is usually consumed comparably quickly by reacting with atomic H or thermal dissociation, hence considered a less concern than the low-temperature pathway.[13]

In dual-fuel ammonia engines, studies have consistently demonstrated increased N_2O emissions with increased ammonia energy share (AES).[14−17] By port injection of ammonia, increased N_2O emissions can offset the GHG emissions for blends with up to 35%[18] or even 40%[14] AES. The increased N_2O emissions in diesel, DME, and natural gas dual-fueled engines have been explained by reduced temperatures accompanying ammonia,[19,20] combustion of ammonia during the expansion stroke,[20] and incomplete combustion.[21] These findings resemble the observations in gas turbines, where N_2O accumulation is highly related to the temperature and wall interaction. In the context of gas turbines, it is demonstrated that N_2O is mainly produced at the flame front and migrates toward the walls, where its concentration levels are related to the wall heat loss.[22,23] For these applications, when the temperature is sufficiently high, the aforementioned consuming reactions of N_2O are active. However, it is found that the equivalence ratio plays a crucial role in the availability of H. A low equivalence ratio leads to a reduced amount of H radicals. Hence, thermal decomposition, strongly dependent on temperature, becomes the predominant consuming reaction. Low concentrations of H are also observed in regions with lower temperatures. Consequently, at temperatures below 1500 K and low wall temperatures, N_2O can accumulate near walls and in recirculation zones. Based on these findings, Hayakawa et al.,[23] in the context of gas turbines, suggested that controlling the equivalence ratio to ensure a sufficient amount of H, especially in low-temperature regions, is important for obtaining low N_2O emissions. The influence of equivalence ratios on the H-containing N_2O consumption reaction is also observed for ammonia blended with a carbon-containing fuel, as is illustrated for methane by Okafor et al.[24] Tang et al.[25] showed that NO_2 and N_2O formation during ammonia oxidation also depends on the equivalence ratio in jet-stirred reactors. The authors related elevated N_2O and NO_2 concentrations in very lean conditions to a high HO_2 concentration, leading to increased OH formation and ammonia dehydrogenation. Higher equivalence ratios led to lower HO_2 formation, inhibiting NO_2 and N_2O produced through $NO + HO_2 \rightleftharpoons NO_2 + OH$ and $NH_2 + NO_2 \rightleftharpoons N_2O + H_2O$.

Ammonia also has a well-demonstrated influence on NO_x emissions, affecting its formation related to fuel-bound nitrogen and its reduction via the thermal De-NO_x mechanism.[26] Ariemma et al.[27] showed that during the combustion of methane/ammonia blends in a cyclic burner, OH radicals generated by methane oxidation can interact with NH_2. This could influence the thermal De-NO_x pathway, leading to a nonlinear relationship with the AES. Consequently, the maximum NO_x emissions were obtained at volumetric fractions of ammonia between 25 and 50%. A later work by Ariemma et al.[28] showed a nonlinear behavior of NO_x and AES for ammonia/alcohol blends. Compared with mixtures of ammonia and methane, the peak in NO_x emission is shifted to higher AES in blends of ammonia and alcohols. As for methane/ammonia blends, it was demonstrated that the nonlinear behavior of NO_x and AES is attributed to the competition between the CO and NH_3 species to consume OH radicals.

Recently, it has also been demonstrated that ammonia could inhibit soot formation through chemical mechanisms, in addition to lowering the amount of carbon in the fuel.[29−34a] In ethylene and premixed *n*-heptane flames, the addition of ammonia has been shown to inhibit the formation of benzene and the production of soot precursors, such as acetylene, due to the interaction between carbon- and nitrogen-containing radicals originating from ammonia decomposition. Instead, the interaction leads to the formation of, among others, cyanide and hydrocarbon amines. Similar observations are made in a dual-fueled ammonia-diesel CI engine by Zaher et al.[35] They reported a monotonic decrease in the level of soot formation as the AES increased. Additionally, the soot particles exhibited a more graphitic nanostructure, which could reduce the rate of soot growth by decreasing carbon bonding at defect sites on the soot surface. They also observed an increase in brake-specific N_2O and NH_3 emissions while a reduction in NO_x emissions. Contrary, Kane and Northrop[36] and Reiter and Kong[9] reported a relatively stable or, in fact, an increase in soot for AES of up to 40%. This behavior was attributed to a lower combustion temperature, an increased local equivalence ratio, and prolonged combustion duration, factors that limited postdiffusion flame soot oxidation.

One promising solution for decreasing unburned NH_3 and N_2O emissions is advancing the injection timing of the diesel pilot fuel.[14,17,20,37] Advanced injection timing could increase the in-cylinder temperature, facilitating complete ammonia combustion and fewer areas with low-temperature combustion. Additionally, when applying direct injection of both fuels, the injection timing of ammonia relative to the pilot injection and the interaction between the sprays influence the burnout rate of ammonia.[38] Ryu et al.[39] found that the injection timing needed to be within a specific range to ensure successful combustion when they mixed DME with ammonia prior to injection. Another innovative solution was proposed by Ichikawa et al.[40] involving a third injection of pilot fuel in a three-layer stratified fuel injection concept. The third injection of *n*-heptane decreased the N_2O emissions as the combustion of the *n*-heptane from this injection reduced the low-temperature regions in the ammonia flame. The third injection also contributed to a higher burnout of ammonia. A repercussion of the higher temperature is higher NO_x emissions related to thermal NO_x.[17]

The presented literature highlights that ammonia influences the formation of NO_x, soot, and N_2O in fuel blends. Additionally, engine performance and emissions depend on

https://doi.org/10.1021/acs.energyfuels.3c02549
Energy Fuels XXXX, XXX, XXX−XXX

operation conditions, such as injection timing. To address the conditional dependencies of high emissions in ICEs, diagnostic maps in the equivalence ratio (ϕ) and temperature (T) space have been numerically created for several hydrocarbon fuels.[41,42] The maps traditionally include regions in which high concentrations of NO_x and soot can be expected. These studies have shown that high temperatures and low equivalence ratios favor high emissions of NO_x. In contrast, soot formation is favored by fuel-rich mixtures (high equivalence ratios) at moderate temperatures. The maps offer a simplified representation of reality, representing the inhomogeneous characteristics of direct injection systems and stratified engine concepts by using a wide set of ideal reactors. They have proven useful when combined with numerical tools like computational fluid dynamics (CFD)[43] and stochastic reactor model[44] calculations. These tools account for inhomogeneities and transient behavior, and, coupled with $\phi-T$ maps, they provide valuable insight into promising operating strategies.[43,45−47] Such studies have suggested that combustion modes, including homogeneous charge CI (HCCI),[45] reactivity-controlled CI (RCCI),[43] and other low-temperature combustion (LTC) strategies,[46] provide conditions favorable for avoiding regions where soot and NO_x are formed in hydrocarbon-based fuels. Further, these maps estimate the emission formation sensitivity to local conditions in a complex mixture formation using complex chemistry in ideal and hence cost-efficient calculations.

To the best of the authors' knowledge, the effect of ammonia in fuel blends has not been explored in the context of $\phi-T$ maps. As the formation of N_2O in ammonia combustion is found to occur mainly at lower temperatures,[13,14] favorable injection strategies when ammonia is included in the fuel could differ from diesel fuel operation. Consequently, comprehending the effect of ammonia on local conditions, as illustrated on these maps, is essential knowledge when designing operation strategies for ICEs.

This work addresses the effect of ammonia on NO_x, soot, and N_2O emissions in dual-fuel ICE. The investigation considers five different fuel blends: pure ammonia, pure *n*-heptane, and three blends of ammonia and *n*-heptane. First, the methodology employed for the numerical kinetic computations using a constant pressure reactor (CPR) with the chemical mechanism from Shrestha et al.[48] is presented. The methodology is further compared and verified with the findings from the numerical work by Kitamura et al.[42] The subsequent sections present and discuss the results systematically for each of the three emissions under consideration, where a new method for analyzing N_2O emissions is proposed. The important chemical reactions leading to the formation of NO_x and N_2O during ignition are identified and discussed. An exploration of the effect of dilution was addressed by decreasing the oxidizer oxygen concentration. Lastly, a joint presentation of all the emissions will be presented on the diagnostic maps and discussed in the context of emissions mitigation.

2. METHODOLOGY

2.1. Chemical Kinetics. This study investigates the combustion of ammonia and *n*-heptane fuels, both separately and in blends, using a numerical approach. *n*-Heptane serves as a surrogate fuel for diesel, as commercial diesel features a complex composition. Ammonia kinetics is an evolving subject. Several studies have investigated ammonia combustion chemistry as a fuel,[25] yet a universally applicable kinetic model for various conditions and fuel blends has yet to be established.[49] Hence, the quantitative accuracy, in particular with respect to N_2O values, is less certain. The chemical mechanism employed in this study comprises 402 species and 2543 reactions and is from the work of Shrestha et al.[48] The mechanism includes both ammonia and *n*-heptane chemistry coupled with the interaction between carbon and nitrogen species. Specifically, the *n*-heptane chemistry is based on the Seidel et al.[50] mechanism, originally developed for fuel-rich premixed *n*-heptane flames. That mechanism has been shown to reproduce NO concentrations well under *n*-heptane oxidation when compared against experimental results in a jet-stirred reactor. For NO_2 concentrations, the trend is captured correctly, yet the values were underpredicted.[48] The mechanism also includes poly-aromatic hydrocarbon pathways as soot precursors used in the soot modeling.[51] The ammonia chemistry is based on a previous mechanism from Shrestha et al.,[52] specifically designed for ammonia oxidation and features an extended validation of ammonia blends. It has shown a good agreement for NO speciation when compared against experiments on fuel-rich ammonia-hydrogen mixed burner stabilized flames.[52] For N_2O concentrations, the trends were captured, but a slight under-prediction was observed. Additionally, it is demonstrated that the mechanism can be integrated with hydrocarbons to predict NO formation in hydrocarbon flames.[48] The carbon−nitrogen chemistry interactions are incorporated from the later work by Shrestha et al.[53] Notably, together with the carbon−nitrogen chemistry, the applied mechanism includes representation of N_2O and NO_x, which Yin et al.[54] demonstrated could be reasonably predicted in their evaluation of chemical mechanisms for ammonia jet-stirred reactor experiments. It should be noted that these experiments were performed at atmospheric pressures, whereas in the present work, a pressure of 60 bar is used. Pan et al.[55] emphasized that further experimental results under engine-relevant conditions are needed to develop applicable robust models for combustion in engines.

2.2. Constant Pressure Reactor Simulations. The creation of the $\phi-T$ diagnostic maps is carried out by modifying the approach of Kitamura et al.[42] Their maps are produced by applying a CPR with a constant temperature constraint. In this study, the temperature is computed as the simulation proceeds to account for transient results and capture the evolving chemistry and temperature effects during the combustion. The LOGEsoft package was used to run the CPR simulations.[56]

The conditions set for the simulations are listed in Table 1. The pressure and final time are set to avoid underpredictions of the emissions in CI engines, following the observations of Kitamura et al.[42] and Akihama et al.[41]

Table 1. Conditions for the CPR Simulations

parameter	value	units
pressure	6×10^6	Pa
final time	2	ms
equivalence ratio	0.1−7.0 ($\Delta\phi = 0.25$)	
initial temperature	700−3000	K

Each simulation generated a data point containing information about the reactor composition under the given initial conditions. The NO and soot emissions presented in the work of Kitamura et al.[42] are located at conditions where the reactor has achieved a fully burned state within 2 ms. However, lower reactor temperatures, which are of particular interest from the perspective of N_2O, are observed only during the ignition

https://doi.org/10.1021/acs.energyfuels.3c02549
Energy Fuels XXXX, XXX, XXX−XXX

process or under dilution. Figure 1 shows the relationship between reactor temperature and N_2O concentration for one

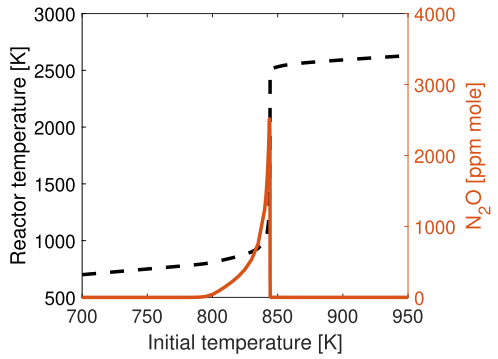

Figure 1. The ignition phase highlighted during the CPR simulations of a 50/50 energy share of ammonia and *n*-heptane at an equivalence ratio of 1.1.

equivalence ratio over different initial temperatures. Notably, the plot shows a significant increase in N_2O concentrations within the temperature range from the initial temperatures (no ignition) to the stable elevated flame temperature. In this study, we define this temperature range as the ignition period. To comprehensively populate the $\phi-T$ diagram with data and represent the ignition process, a different approach is proposed for these conditions. Specifically, the results for the ignition period are gathered at times of less than 2 ms from one transient simulation for each equivalence ratio. For these simulations, the initial temperature was set as the minimum initial temperature that provides fully burned conditions after 2 ms for the specific equivalence ratio. Consequently, we denote the reactor temperature at the end of this simulation as $T^{\min}_{\mathrm{CPR@2ms}}$ and is indicated by a red line in the results. The red line and the available data points for the case of the 50/50 energy share of ammonia and *n*-heptane are presented in Figure 2. At temperatures higher than $T^{\min}_{\mathrm{CPR@2ms}}$, we obtained results from CPR simulations at 2 ms when a fully burning state is achieved. At reactor temperatures lower than $T^{\min}_{\mathrm{CPR@2ms}}$, we collected data at times earlier than 2 ms. These results consistently represent the transient ignition process. Between each of the data points, a linear interpolation was applied.

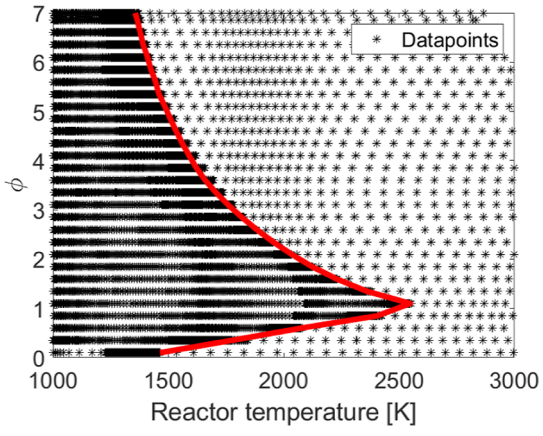

Figure 2. Data points for the 50/50 energy share of ammonia and *n*-heptane. The red line corresponds to $T^{\min}_{\mathrm{CPR,2ms}}$. Results at temperatures higher than $T^{\min}_{\mathrm{CPR,2ms}}$ are obtained at a reaction time of 2 ms. At lower temperatures, the results are obtained at different times <2 ms.

Three different blends of ammonia and *n*-heptane were selected based on the AES with the following formula

$$E_{\mathrm{NH_3}} = \frac{Y_{\mathrm{NH_3}}\mathrm{LHV}_{\mathrm{NH_3}}}{Y_{\mathrm{NH_3}}\mathrm{LHV}_{\mathrm{NH_3}} + Y_{n\text{-}\mathrm{C_7H_{16}}}\mathrm{LHV}_{n\text{-}\mathrm{C_7H_{16}}}} \quad (1)$$

where $E_{\mathrm{NH_3}}$ is the energy share of ammonia, $\mathrm{LHV}_{\mathrm{NH_3}}$ and $\mathrm{LHV}_{n\text{-}\mathrm{C_7H_{16}}}$ are the lower heating values of ammonia (18.6 MJ/kg) and *n*-heptane (45.5 MJ/kg), and $Y_{\mathrm{NH_3}}$ and $Y_{n\text{-}\mathrm{C_7H_{16}}}$ are the mass fractions of the two fuels. The mole and mass fractions for each case are presented in Table 2. In all the cases, air was used as the oxidizer, with 21% oxygen and 79% nitrogen on a molar basis. In addition to the five cases in Table 2, the dilution effect was analyzed for case 3, where the oxidizers' oxygen mole fraction was changed to 10% with nitrogen as diluent.

2.3. Emission Identification. NO_x and N_2O emissions are presented in ppm on a molar basis, where NO_x is the sum of NO and NO_2. The soot formation is obtained with the soot model based on the method of moments and detailed kinetics approach proposed by Mauß.[51] The output data for soot formation is soot yield and, hereby, soot mass fraction. For the N_2O and NO_x emissions, an additional investigation on the most influential reaction pathways leading to the formation and consumption of the respective species. The differentiation of various mechanisms responsible for NO_x production was addressed by conducting a reaction pathway analysis, where the origin of species and most contributing pathways were examined.

3. VERIFICATION

To verify the numerical setup, a comparison of the NO and soot yield obtained for *n*-heptane with the numerical results of Kitamura et al.[42] (reference study) was performed. Since the present study's method involves temperature calculation as the simulation proceeded, some discrepancies compared to the results of the reference study were expected. Therefore, calculations with a constant temperature constraint were also performed to enable a comparison. The comparison results are presented in Figure 3a,b, where the red contour lines indicate the present study's results and the black contour lines are retrieved from the reference study. The results show that both approaches produce reasonably comparable NO concentrations with the reference study. For the soot formation, although the soot formation region is situated at a similar location to Kitamura et al.,[42] the levels of soot yield are lower in the present study. It is observed that the constant temperature constraint produced a more significant deviation in soot yield compared to the results of the reference study than when computing the temperature. This discrepancy highlights the effects of differences in the kinetic mechanism and soot modeling. Despite this, the trends observed were similar to those obtained in the reference study.

The 500 and 5000 ppm of NO contour trends exhibited similar behavior as in the reference study, though it should be noted that the equivalence ratio interval investigated in the present study was between 0.1 and 7.0, whereas in Kitamura et al.,[42] the equivalence ratio goes down to 0. A half-circle trend similar to that in the reference case is assumed for equivalence ratios lower than 0.1. Besides this behavior, the NO limits in the present study were located at slightly lower equivalence ratios than the reference study, possibly due to the present study's use of a $\Delta\phi$ of 0.25, compared to Kitamura et al.'s[42] $\Delta\phi = 0.5$.

https://doi.org/10.1021/acs.energyfuels.3c02549
Energy Fuels XXXX, XXX, XXX−XXX

Table 2. Composition of the Selected Ammonia/*n*-Heptane Blends

case number	energy fraction, E_i [%]		mass fraction, Y_i [—]		mole fraction, X_i [—]	
	n-C_7H_{16}	NH_3	n-C_7H_{16}	NH_3	n-C_7H_{16}	NH_3
1	100	0	100	0	100	0
2	80	20	62.0517	37.9483	21.7479	78.2521
3	50	50	29.0172	70.9828	6.4967	93.5033
4	20	80	9.2722	90.7278	1.7074	98.2926
5	0	100	0	100	0	100

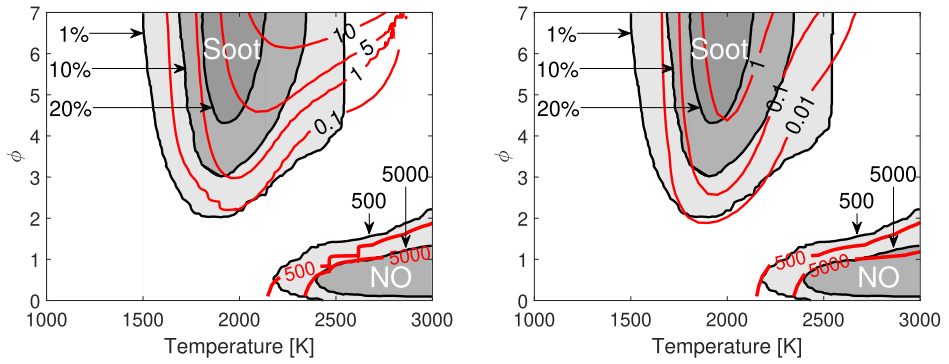

(a) Computed temperature. (b) Constant temperature.

Figure 3. Comparison between the results obtained in this work and by Kitamura et al.[42] (a) Shows the results with the method applied in this work. (b) Shows the results with a method similar to that in the reference study. The red lines represent the 500 and 5000 ppm limits of NO and the soot yield limits for 0.1, 1, 5, and 10%.

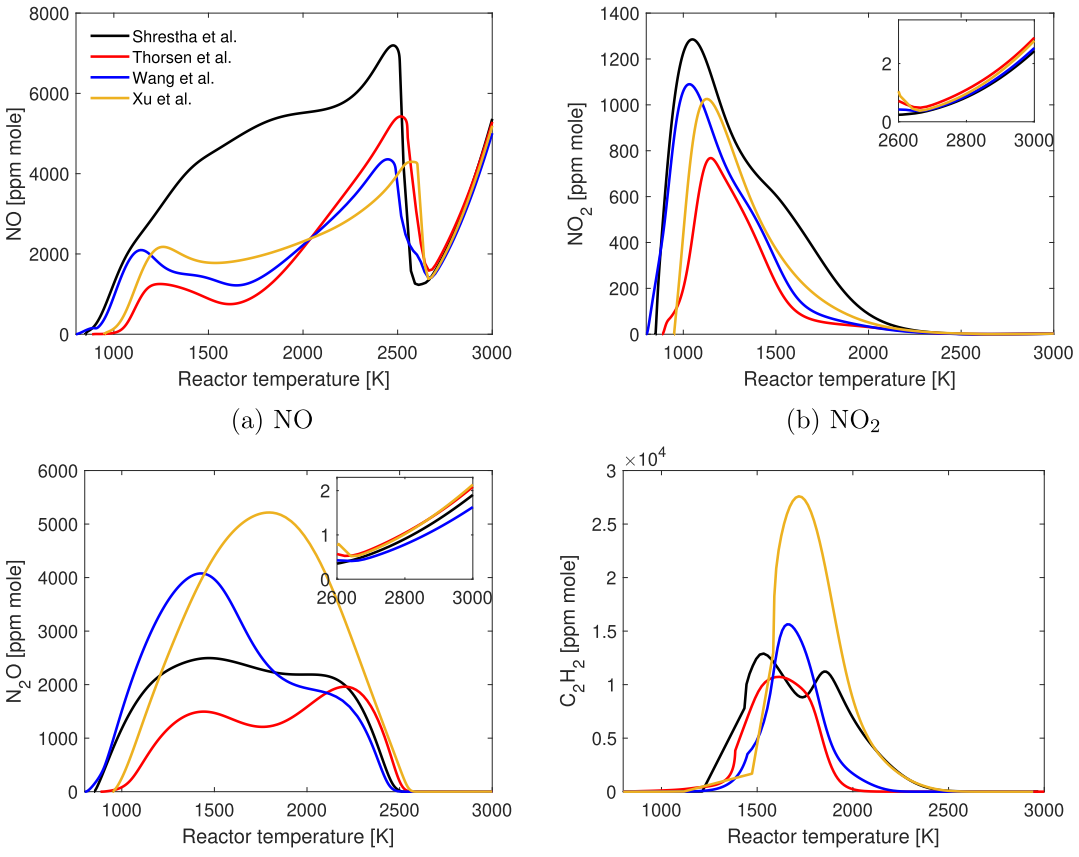

(a) NO (b) NO_2

(c) N_2O (d) C_2H_2

Figure 4. NO, NO_2, N_2O, and C_2H_2 concentrations for case 3 computed with four different mechanisms; Shrestha et al.,[48] Thorsen et al.,[57] Wang et al.,[58] Xu et al.[34] NO, NO_2, and N_2O concentrations are gathered for ϕ = 1.1, while C_2H_2 is obtained at ϕ = 6.

https://doi.org/10.1021/acs.energyfuels.3c02549
Energy Fuels XXXX, XXX, XXX−XXX

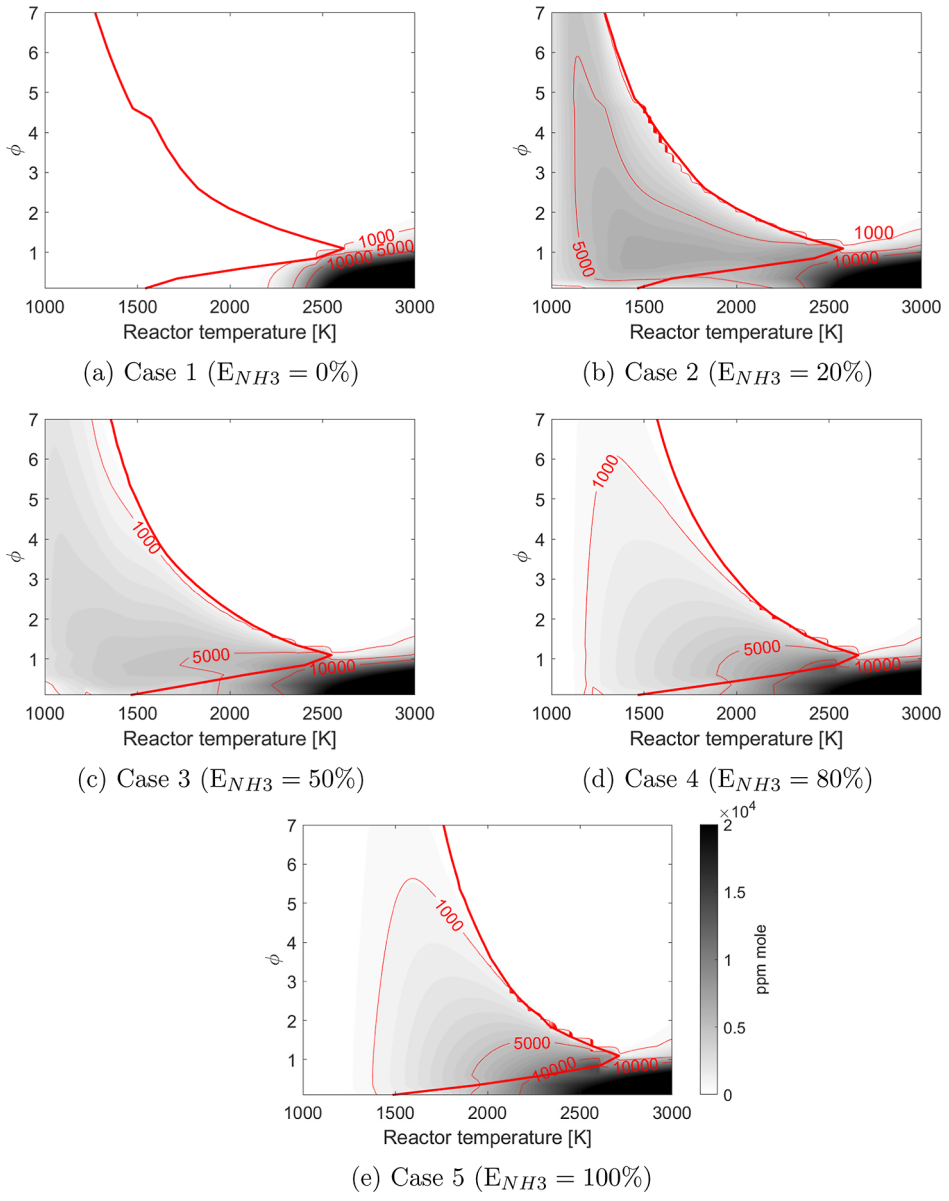

(a) Case 1 ($E_{NH3} = 0\%$) (b) Case 2 ($E_{NH3} = 20\%$)

(c) Case 3 ($E_{NH3} = 50\%$) (d) Case 4 ($E_{NH3} = 80\%$)

(e) Case 5 ($E_{NH3} = 100\%$)

Figure 5. NO_x emissions represented on $\phi-T$ maps for the five cases. 1000, 5000, and 10,000 ppm limits are presented with a thin red contour line. NO_x values above 500 ppm are visible. The thick red line represents $T^{min}_{CPR,2ms}$.

The mechanism applied in this work has shown its ability to reproduce reliable NO concentrations both for *n*-heptane oxidation in a jet-stirred rector[48] and for a fuel-rich ammonia-hydrogen oxidation in a burner-stabilized flame.[52] Furthermore, given its ability to reproduce the work of Kitamura et al.,[42] the calculations of the present study are expected to produce reasonable results with respect to NO.

As stated earlier regarding the soot predictions, Figure 3a shows differences as well. Focusing on the method applied in the present study, the isoline of soot mass fractions overlaps with the reference study, but the values show an order of magnitude differences. The discrepancies in values grow as the equivalence ratios increase, given that the present study's soot yield limits shift more rapidly toward higher equivalence ratios. It can be seen from Figure 3a that the trends for the 0.1 and 1% soot isolines are relatively similar to the reference limits of 1 and 10%, respectively. Thus, qualitatively, the trend in the sooting tendency is comparable.

To assess the impact of different chemical mechanisms on the $\phi-T$ diagrams, we compared the formation of NO, NO_2, N_2O, and acetylene (C_2H_2) across four distinct mechanisms. Acetylene is included as it is a soot precursor and can be used to indicate the potential to produce soot.[42] Soot formation is primarily observed at higher equivalence ratios; hence, an equivalence ratio of 6 is chosen for the comparison of acetylene, while for NO, NO_2, and N_2O, an equivalence ratio of 1.1 is selected. Figure 4 displays the comparison with the four mechanisms: Shrestha et al.[48] (402 species and 2543 reactions), Thorsen et al.[57] (1369 species and 6314 reactions), Wang et al.[58] (74 species and 495 reactions), and Xu et al.[34b] (69 species and 389 reactions).

The comparison shows minor differences in levels and trends among the mechanisms at high temperatures (above 2650 K). At temperatures below 2600 K, differences both in trend and in levels are observed. These temperatures correspond to the ignition phase when the equivalence ratio is 1.1, while at an

https://doi.org/10.1021/acs.energyfuels.3c02549
Energy Fuels XXXX, XXX, XXX−XXX

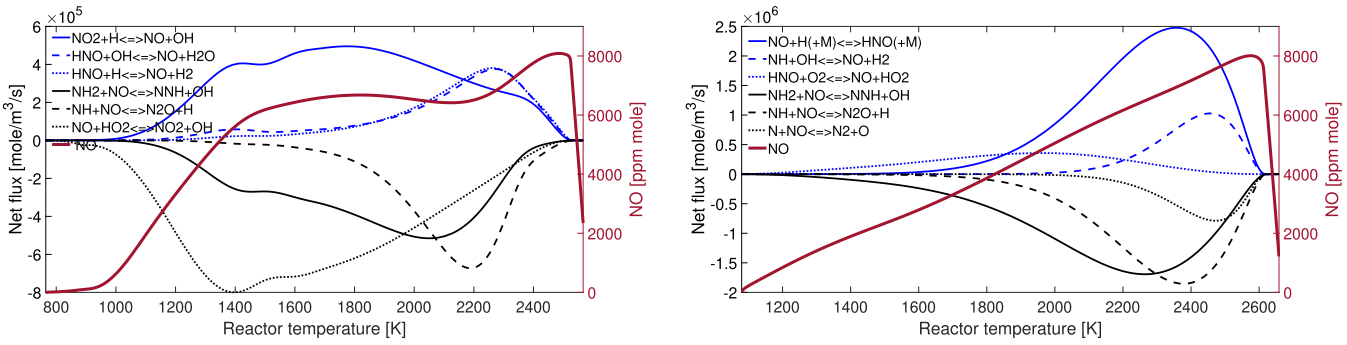

(a) Case 2 ($E_{NH3} = 20\%$) (b) Case 4 ($E_{NH3} = 80\%$)

Figure 6. NO formation and consuming pathways within the ignition phase for cases 2 and 4 at ϕ = 1.1. The initial temperature assuring complete combustion in 2 ms was for case 2, 765 K, and for case 4, 1080 K.

equivalence ratio of 6, the ignition phase is at temperatures below 1500 K.

Regarding C_2H_2 concentrations, the mechanism from Xu et al.[34] yields higher peak values than the three other mechanisms. The Shrestha et al.[48] mechanism shows the widest region with elevated concentrations, which could be favored to avoid underpredictions. In terms of NO_x emissions, Shrestha et al.[48] give higher values during the ignition phase for NO and NO_2 compared to the other mechanisms, while all mechanisms show peak concentrations in the temperature range around 2500 K. Based on these findings, NO_x concentrations could be lower during the ignition phase employing another mechanism. N_2O concentrations follow similar trends and values for both Shrestha et al.[48] and Thorsen et al.,[57] while Xu et al.[34] show a single peak and deviate from the other mechanisms. Wang et al.[58] show one peak; however, a behavior somewhat similar to the two more detailed mechanisms toward the end of the ignition phase is observed.

To summarize, as the concept of $\phi-T$ maps is a simplistic representation of reality, trends are the most important factor, as concentration levels will be affected by real-world phenomena such as turbulence and residual gases, which are not considered here. Hence, the numerical methodology and the choice of using the mechanism of Shrestha et al.[48] are regarded as valid for their purpose. Calculations performed by applying the constant temperature constraint are provided in the Supporting Information S.A.

4. RESULTS

The following section presents the obtained results and discusses how to interpret them. First, the evolution of the NO_x region is discussed, differentiating the contributions from the thermal and fuel formation processes as the amount of ammonia in the fuel blend increases. Second, relevant soot region depreciation is presented. Then, the introduced N_2O emission regions, accompanied by influential formation pathways and observed trends, are presented for varying fuel compositions. Finally, all emission regions are combined and shown on one map for each case.

4.1. NO_x Formation. The obtained NO_x emissions for cases 1 to 5, under the conditions listed in Table 1, are presented in Figure 5. The NO_x levels are presented with equal color grading for each case, where the limit is set such that parts per million levels between 500 and 20,000 are shown with varying shading. Thin red contours are included to mark 1000, 5000, and 10,000 ppm levels.

The first observation is that high NO_x concentration levels are located at high temperatures and low equivalence ratios, which is typical for formation through the thermal NO mechanism. For all cases, levels above 10,000 ppm are located in a region between 2200 and 3000 K at lean to stoichiometric conditions. For temperatures above 2600 K, the 10,000 ppm contour is indistinguishable, given the verification uncertainties discussed in Section 3. This is true for all five fuel blends, implying a weak fuel dependency at these temperatures. This observation suggests, for these conditions, that the thermal NO mechanism is the primary mechanism contributing to NO_x emissions, with negligible or minor differences in other NO_x-producing mechanisms. For conditions below 2600 K, the 10,000 ppm contour tends to shift toward lower temperatures with an increasing ammonia fraction. At reactor temperatures above $T^{min}_{CPR,2ms}$, all cases' NO_x levels are located at high temperatures and low equivalence ratios, with no regions exceeding 500 ppm for equivalence ratios higher than 1.5.

NO_x emissions outside of the high concentration area (values above 10,000 ppm) are predominantly observed during ignition, and the concentrations in this region depend on the fuel. For the case of pure *n*-heptane, the only region featuring over 500 ppm levels is located at high temperatures and low equivalence ratios. For the cases involving ammonia, an area with elevated NO_x concentrations extends into the ignition region. In this region, the highest concentrations are located at equivalence ratios below two and decrease in value toward higher equivalence ratios. The ratio between ammonia and *n*-heptane impacts the NO_x emissions within this region. Figure 5 shows that the part of NO_x at lower temperatures is most apparent for case 2, whereas both the values and the size of this region diminish with a higher ammonia concentration. This resembles the observations for methane/ammonia combustion in Ariemma et al.,[27] where maximum NO_x emissions were observed when the ammonia volumetric fraction was between 25 and 50%. Despite this, the behavior and shape of this region are similar in all cases containing ammonia.

Figure 6 shows the three-most net-forming and consuming reactions, respectively, during the ignition period for cases 2 and 4. Toward high temperatures (late in the ignition phase), similar peak NO values are observed in both cases, slightly above 8000 ppm, before it is consumed. At lower temperatures, the concentrations differ from each other. Due to the reaction between NO_2 and H creating NO and OH, the NO concentration has a wide region of high levels when the hydrocarbon fuel is present at higher concentrations. This leads

https://doi.org/10.1021/acs.energyfuels.3c02549
Energy Fuels XXXX, XXX, XXX−XXX

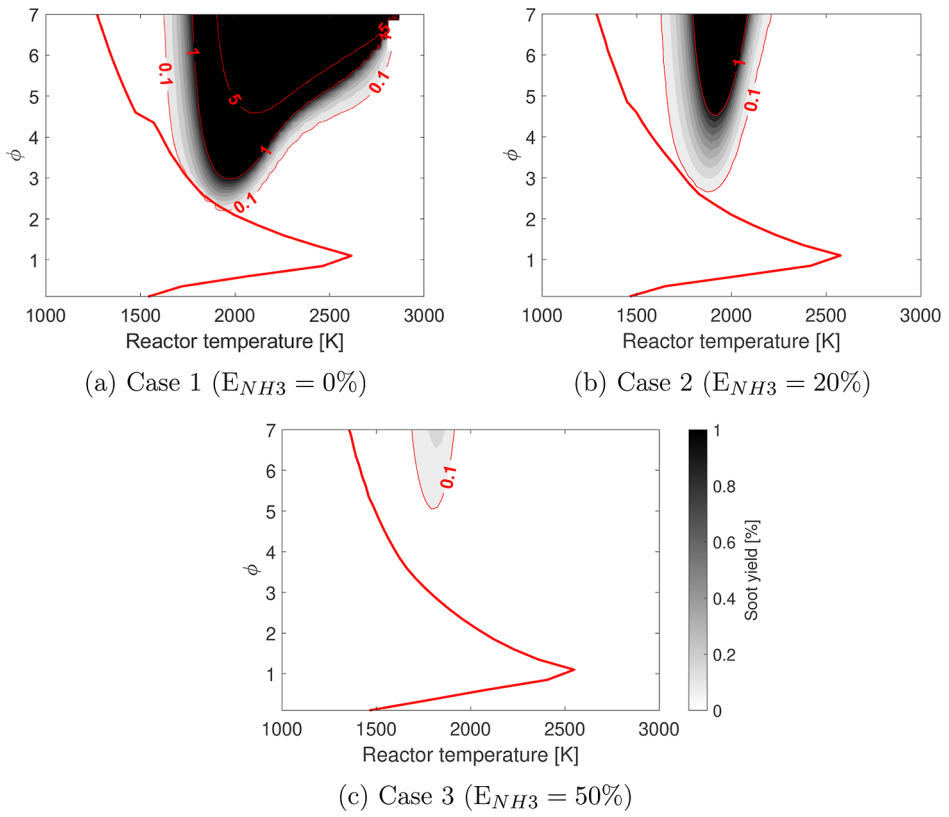

Figure 7. $\phi-T$ map with soot yield for cases 1, 2, and 3. The red lines represent the 0.1, 1, and 5% soot yield limits. The color-grading is equal in all three figures.

to higher emission levels located early in the ignition phase for case 2 compared to case 4, explaining why higher NO_x concentrations are observed for lower ammonia concentrations. Except for this pathway, the two remaining contributing pathways are related to the formation through HNO reacting with OH, H, or a third body. Pathways, including HNO, are linked to the oxidation of NH_3 and are expected to appear as ammonia gets introduced into the fuel.[26] First, NH_3 oxidizes to amidogen (NH_2). Then amidogen is converted to NO through HNO by a reaction sequence, including the reactions observed in Figure 6. An increase in AES leads to an increased NO formation, which can be observed by noting the order of magnitude differences at the left *y*-axis between the two figures in Figure 6. However, the net NO formation early in the ignition phase decreases with increasing ammonia, despite the higher formation rate. This is mainly due to the increasing impact of the thermal De-NO_x mechanism, where NO gets consumed through interactions with NNH and NH_2 via the thermal DeNO_x pathways discussed in Glarborg et al.[26] This can be observed in Figure 6, where it can be seen that $NH_2 + NO \rightleftharpoons NNH + OH$ retains the NO formation in case 4, while in case 2, it exhibits a significantly lower rate. The pathway analysis shows that consuming reactions are active mainly late in the ignition process, toward equilibrium, underlining the benefits of achieving total combustion of the fuel. If the ignition process is interrupted, for example, when quenched, high emissions could be the result.

In addition to the mentioned pathways, it was observed that the origin species for NO changes with fuel composition. It was found that the formation through HNO, thereby through NH_3 oxidation (fuel NO), contributes to a higher percentage as the ammonia content increases. This is expected as more nitrogen is bound in the fuel. At the same time, the contribution from carbon-containing species decreases, indicating a decrease in the level of prompt NO formation with a reduced amount of hydrocarbons in the fuel. The decrease in prompt NO contribution is also evident as the amount of NH produced through NCO + H decreases. Furthermore, as mentioned in the previous section, the thermal De-NO_x mechanism's impact is indicated, as the amount of NO consumed to end up as NNH and N_2 increases with the ammonia energy fraction.

4.2. Soot Formation. The results presented in Figure 7 show soot yields for cases 1, 2, and 3. The color bar is set equally for all the cases to highlight the fuel dependency. Similar in all the cases, the thin red contours present the 0.1, 1, and 5% soot yield limits. For the two cases with the highest ammonia content, the emissions are below 0.1% over the whole range of conditions, hence not included in this section. Figure 8 is created to display how the 0.1% isocontour for cases 1, 2, and 3 changes with fuel composition. This limit is chosen based on the similarities with the 1% sooting limit from Kitamura et al.[42] The comparison shows that the region embraced by the 0.1% limits becomes narrower and shifts to higher equivalence ratios when the ammonia concentration increases. For case 3, an equivalence ratio of 5.05 is needed to reach the 0.1% soot yield limit, while for cases 1 and 2, this limit is reachable for equivalence ratios of 2.20 and 2.65, respectively.

The results presented in Figures 7 and 8 indicate that soot formation is highly dependent on the fuel composition and the number of carbons in the fuel. This is expected because soot formation results from the chemical reaction between carbons in the fuel, leading to the formation of aromatic rings and polycyclic aromatic hydrocarbons, which eventually solidify into particles. In addition to the reduced carbon, recent studies have

https://doi.org/10.1021/acs.energyfuels.3c02549
Energy Fuels XXXX, XXX, XXX−XXX

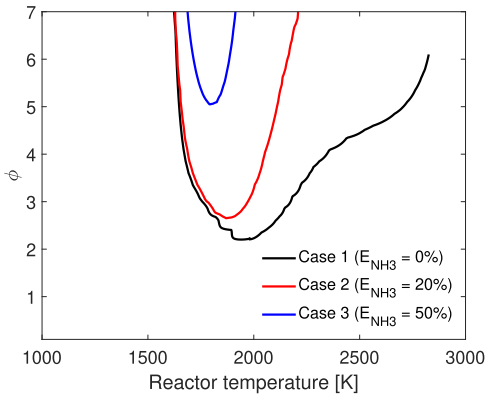

Figure 8. 0.1% soot formation limit for cases 1, 2, and 3.

shown that N-radicals react with C-radicals, effectively inhibiting carbon atoms from engaging in soot precursor formation. For case 1, where the fuel consists of pure *n*-heptane, the soot formation potential is considerable. As the ammonia content increases, the formation potential reduces, and for cases 3 to 5, it becomes of little concern.

These findings share similarities with the correlation between oxygenated fuels and soot formation observed in Kitamura et al.[42] They demonstrated that fuels with a higher oxygen content exhibited a reduced tendency to produce soot compared with aliphatic and aromatic fuels. The atomic bounded oxygen in the fuel contributed to the decrease in the formation of soot precursor species and resulted in a narrower and smaller soot formation region, similar to what is observed with ammonia addition.

However, as the concern of soot reduces with ammonia, other emissions can become of concern. An increased amount of unburned ammonia was observed under rich conditions with ammonia increase. Another consequence of nitrogen-containing radicals reacting with carbon-containing radicals is the possible

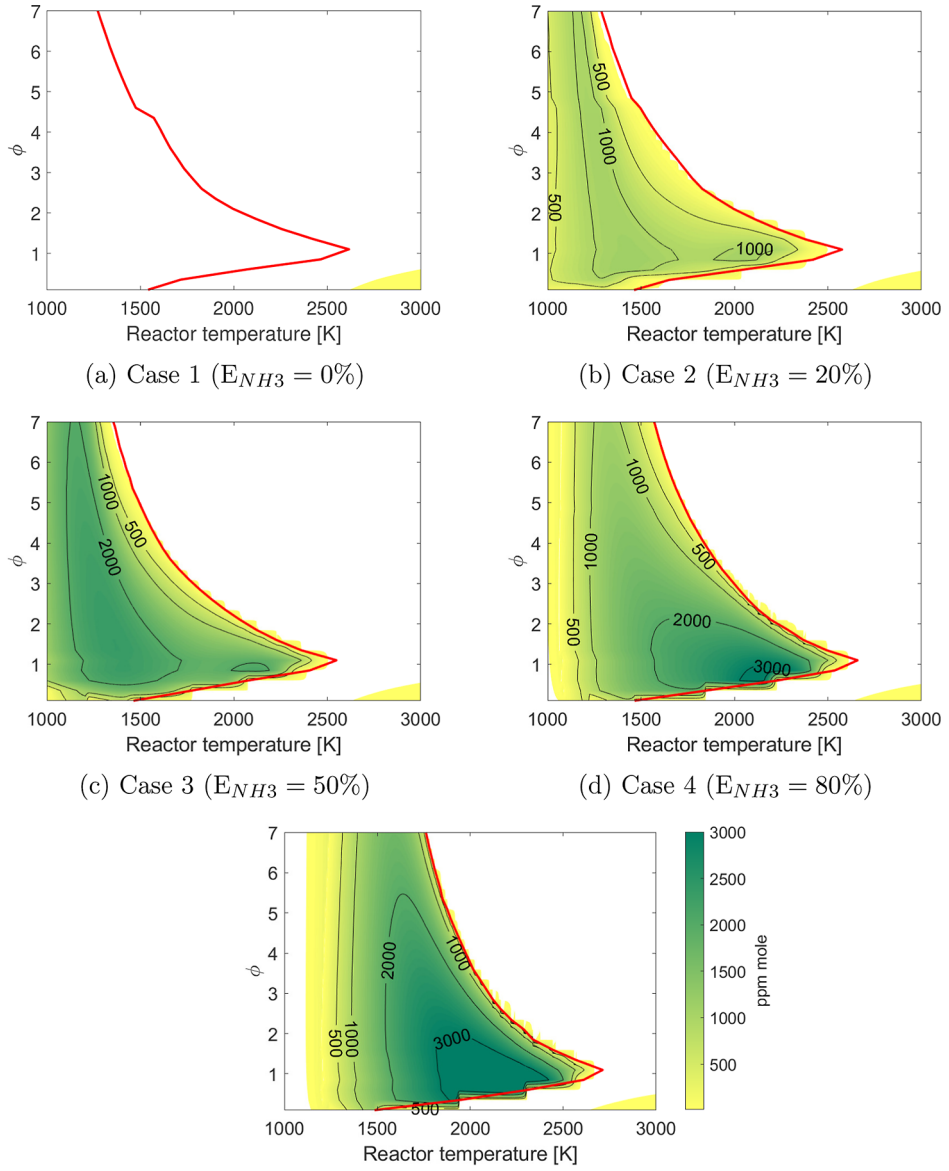

(a) Case 1 ($E_{NH3} = 0\%$)

(b) Case 2 ($E_{NH3} = 20\%$)

(c) Case 3 ($E_{NH3} = 50\%$)

(d) Case 4 ($E_{NH3} = 80\%$)

(e) Case 5 ($E_{NH3} = 100\%$)

Figure 9. $\phi-T$ map with N_2O concentrations for all the cases. The color scale is equal in all five figures.

https://doi.org/10.1021/acs.energyfuels.3c02549
Energy Fuels XXXX, XXX, XXX−XXX

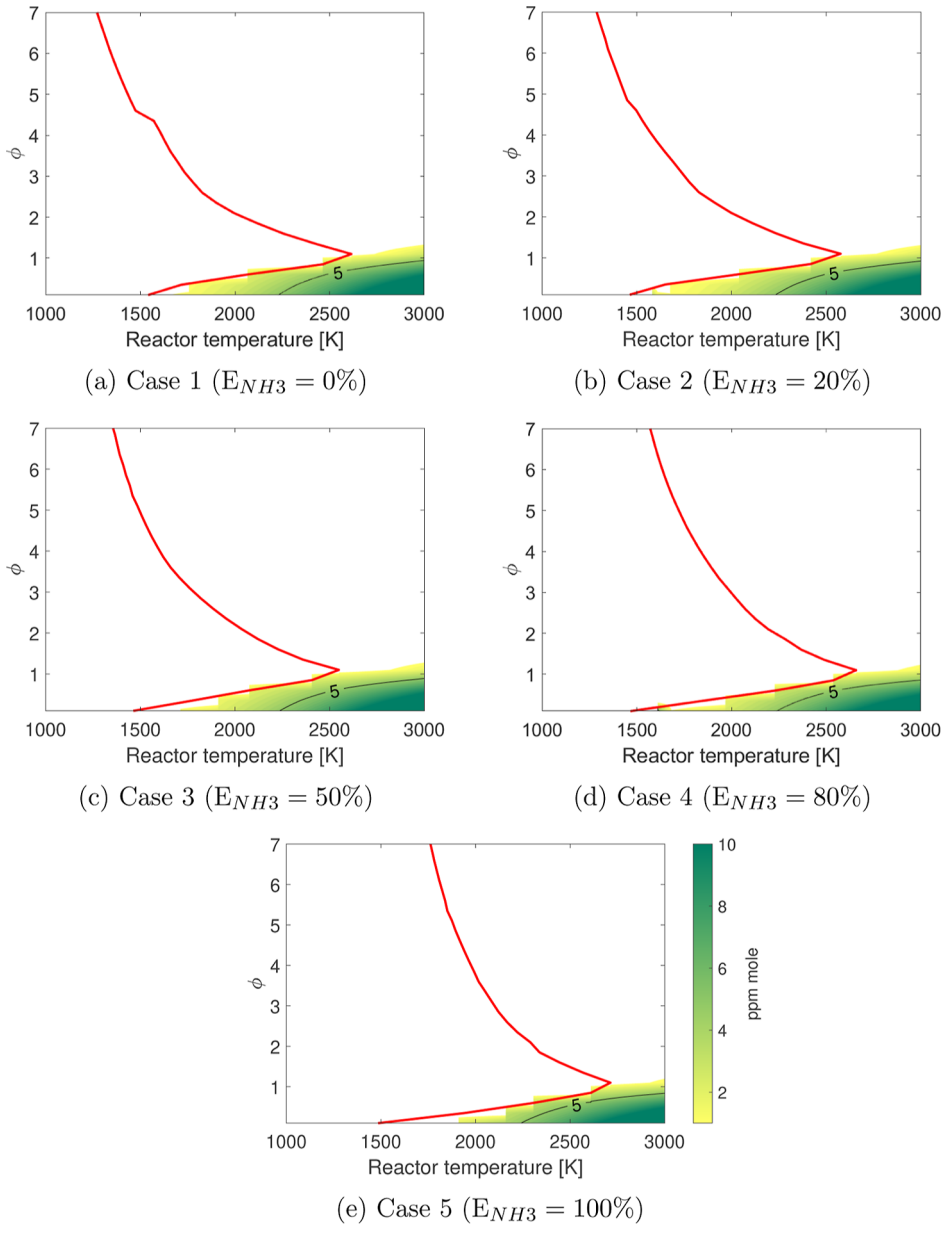

Figure 10. $\phi-T$ map with N_2O concentrations for equilibrium results (results after the red line) for cases 1−5. The color-grading is equal in all five figures.

increased production of cyanides, including the highly toxic compound hydrogen cyanide (HCN).[31] In the present study, the introduction of ammonia into the fuel leads to the emergence of a region with higher concentrations of HCN (Supporting Information S.C). To generate a significant amount of HCN using pure *n*-heptane, temperatures above 2400 K and high equivalence ratios greater than 3 are required. However, when ammonia is added to the fuel, the presence of nitrogen becomes more apparent, and a region with higher concentrations of HCN is observed at lower temperatures. This region overlaps with the region where soot is produced, and it occurs at equivalence ratios of 2 and above, as well as medium to high temperatures (≥1400 K). Among the different cases considered, case 2 shows the highest potential for producing elevated emissions of HCN. Interestingly, as the amount of ammonia in the fuel increases, the concentrations of HCN in the same region decrease.

During dual fuel operation, injecting both fuels simultaneously or at different timings can create different local compositions and conditions for the fuel and the oxidizer within the combustion chamber. The above-presented results consider a homogeneous mixture of ammonia and *n*-heptane with a global equivalence ratio, hence presenting certain limitations. In an engine cylinder, within the diffusive flame of the hydrocarbon pilot fuel, soot can be created under locally rich conditions, regardless of a low global equivalence ratio. This aligns with previous works' conclusion that an increase in soot emissions, with the inclusion of ammonia to a certain amount, could be linked with the reduced combustion temperature ammonia brings, leading to reduced soot oxidation in the later stages of the diesel flame.[36]

4.3. N_2O Formation. The N_2O concentrations obtained for the diagnostic maps are presented in Figure 9. With varying shading, the figure shows molar concentrations ranging from 10 to 3000 ppm. Levels exceeding 3000 ppm are dark green.

https://doi.org/10.1021/acs.energyfuels.3c02549
Energy Fuels XXXX, XXX, XXX−XXX

Additionally, black contour lines represent the 500, 1000, and 3000 ppm levels. The results show that most of the higher N_2O concentrations are obtained at temperatures lower than $T^{min}_{CPR,2ms}$, i.e., during the ignition period, apart from in case 1. The magnitude of the values within this region increases as the amount of ammonia in the fuel increases, ranging from slightly above 1000 ppm in case 2 to levels exceeding 3000 ppm by moles for the two cases with the highest ammonia concentration. Additionally, the N_2O region shifts to higher temperatures as the AES increases, as a result of the higher ignition temperature required. One interesting feature of the results is that in cases 2 and 3, two peaks of N_2O concentrations are observed during the ignition phase. This phenomenon is addressed later in this section. For pure *n*-heptane, all concentrations exceeding 10 ppm are located at high temperatures and low equivalence ratios. This region behaves independently of the fuel mixture, highlighted in Figure 10, which displays the results where stable elevated reactor temperatures are achieved, i.e., at temperatures higher than $T^{min}_{CPR,2ms}$. The figure shows that all concentrations above 5 ppm are located under similar conditions. The placement of this region coincides with the thermal NO region, originating from the splitting of NO by the reaction 2 NO ⇌ N_2O + O.

The fuel-independent behavior observed in Figure 10 suggests that if the ignition process does not get interrupted and complete combustion is assured, negligible differences in N_2O formation between the fuels could be obtained. Similar observations are made when the oxidizer is diluted, as will be discussed in Section 4.5. In gas turbines, low concentrations of N_2O are achieved when there is a sufficient amount of atomic hydrogen available and high temperatures, allowing contributions from thermal dissociation.[23] This implies that the increased N_2O emissions in dual-fuel ammonia engines[14,20] originate from phenomena that occur during ignition interruption, flame extinction, or reactions at low temperatures. While incomplete fuel burning is undesirable in a regular engine operation, there are situations within the engine cylinder where the combustion process can be interrupted during ignition, for instance, wall quenching. The results further show that as more ammonia is introduced, the higher the concentrations within the ignition phase region, hence increasing the potential of emitting more N_2O if the combustion is disturbed. Elevated N_2O concentrations during the ignition period are also observed for *n*-heptane, although significantly weaker than in cases involving ammonia.

The results in Figure 9 show that, close to stoichiometric conditions, two peaks of N_2O within the ignition phase region are obtained for 20 and 50% of AES (cases 2 and 3). Figure 11 illustrates this behavior, displaying the N_2O concentration throughout the ignition period at an equivalence ratio of 1.1 for all cases. The results indicate that when the ammonia content in the fuel is the primary source of energy, a single peak is observed. However, when the hydrocarbon fuel contribution increases, the N_2O curve exhibits a flattened behavior and results in two peaks for cases 2 and 3.

To understand the underlying kinetics behind the N_2O behavior in the ignition period, we investigated the reaction pathways leading to N_2O formation and consumption. In this analysis, two species, CH_2O and OH, were selected as indicators for the occurrence of low- or high-temperature kinetics, respectively.

Figure 12 displays the three primary reaction pathways responsible for N_2O formation, along with the three main

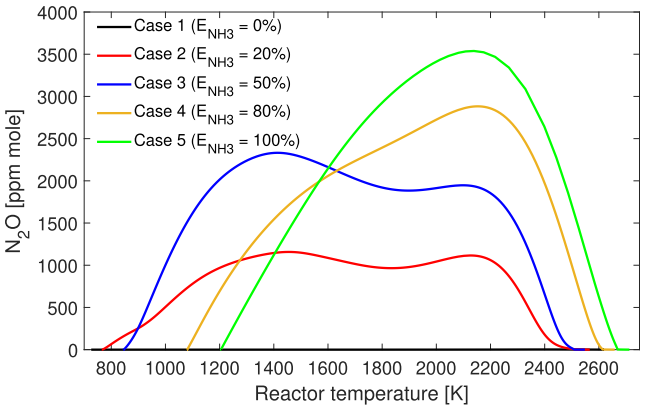

Figure 11. N_2O concentration during the ignition phase for ϕ = 1.1.

consumption pathways, for each case during the ignition period at an equivalence ratio of ϕ = 1.1. Additionally, it shows the N_2O concentration for each case and includes an indication of the region where high-temperature kinetics become active. The start of this region is defined as the point where the temperature-integrated OH reaches 5% of the total OH integrated over the entire ignition period.

To explore the behavior of the two peaks in cases 2 and 3, the relation between the N_2O, CH_2O, and OH concentrations during the ignition period is presented in Figure 13. The figure shows that CH_2O and OH are present, however, in different temperature ranges. Notably, the first peak of N_2O is located at the same temperature range as the peak of the CH_2O concentration, which suggests the presence of low-temperature chemistry. The second peak coincides with the OH peak, indicating high-temperature chemistry. In case 4, a similar effect is observed, where a less steep increase in N_2O is observed between the peaks of the CH_2O and OH concentrations.

The reaction primarily responsible for the first peak is NH_2 + NO_2 ⇌ N_2O + H_2O. Toward the second peak, a contribution of NH + NO ⇌ N_2O + H arises. The two reactions are active across all cases in the present work, and it was observed that the limiting species for the two reaction pathways are the NH and NH_2 molecules, as there is always a surplus of NO and NO_2 when the specific reactions are active.

The NH_2 + NO_2 pathway has a significantly higher contribution at lower temperatures for cases 2 and 3 compared to cases with both higher and lower AES, as evidenced by the zoomed-in plot in Figure 12. One of the reasons for the heightened contribution in this region is the reduced recycling of NH_2 to NH_3. Specifically, the consumption of NH_2 to form NH_3 is much lower toward the first peak compared to the region between the first and second peaks. In case 2, around 10% of NH_2 recycles directly to NH_3 until the first peak, whereas recycling is substantially higher (around 50%) between the two peaks. Case 3 shows a similar behavior, with recycling percentages of 12 and 56%, respectively. The primary pathways for recycling NH_2 to NH_3 are NH_2 + H_2O ⇌ NH_3 + OH and NH_2 + H_2 ⇌ NH_3 + H. Toward the first peak, most of H is attracted by the carbon species, while only around 8% in case 2 and 6% in case 3 end up as H_2, which can be used in the recycling to NH_3 directly or first through H_2O formation. Between the two peaks, around 18% (case 2) and 24% (case 3) of H end up as H_2. Notably, other significant consumers of H, such as OH and HO_2, are considerably less consumed by carbon-related species during this time. In case 4, the recycling of NH_2 to NH_3 toward

https://doi.org/10.1021/acs.energyfuels.3c02549
Energy Fuels XXXX, XXX, XXX−XXX

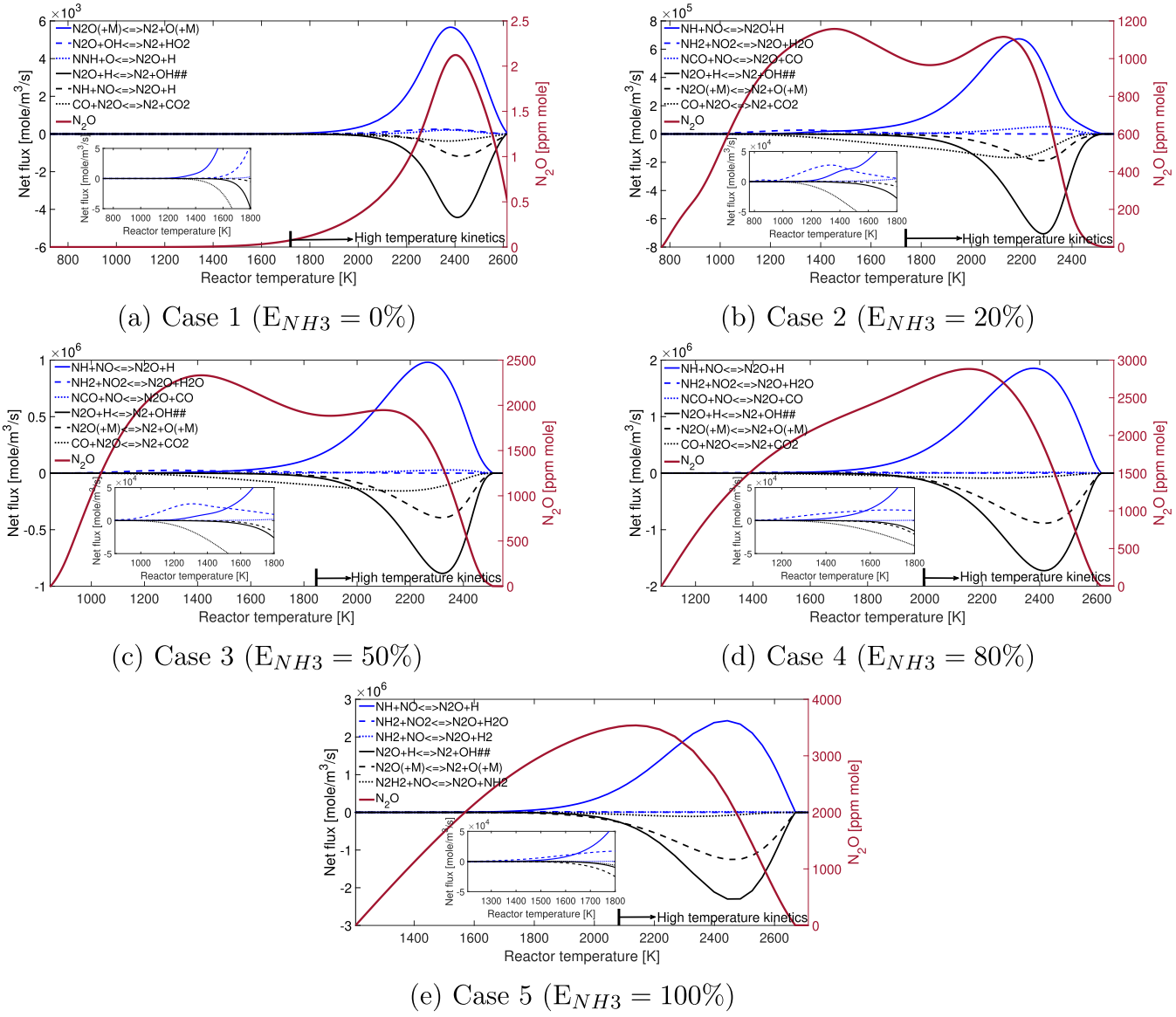

Figure 12. Three most producing and consuming reactions during ignition for cases 1−5, at ϕ = 1.1. Blue lines represent the formation pathways. Black lines represent consuming pathways.

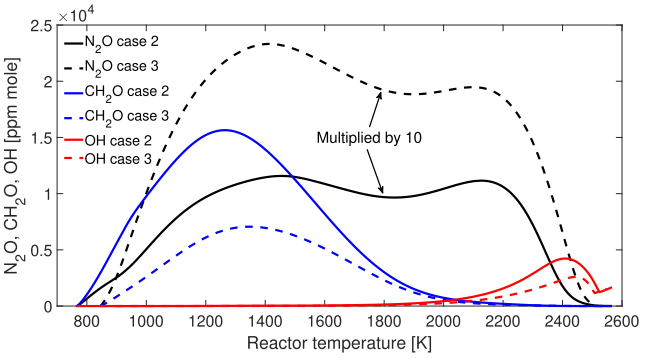

Figure 13. CH_2O, OH, and N_2O concentration during the ignition phase for cases 2 and 3 at ϕ = 1.1. The N_2O concentration is multiplied by 10 for visual purposes.

the peak of CH_2O is roughly twice as much as in cases 2 and 3. This indicates that hydrocarbons in the fuel hinder the recycling of NH_2 to NH_3 toward the first peak, resulting in a higher percentage of NH_2 available to react and form N_2O.

For the two cases featuring two peaks in N_2O, an elevated equilibrium temperature at 2 ms can be achieved from initial temperatures around 770 K in case 2 and 845 K in case 3. When the initial temperature is increased to 1250 K, only one N_2O concentration peak is present across all cases. This underlines the impact of the low-temperature chemistry effects associated with the hydrocarbon fuel.

As stated, the early formation of N_2O is mainly due to the interaction between NH_2 and NO_2. This occurs for all equivalence ratios and is the main contributor to N_2O at lower temperatures during the ignition (≤1400−1500 K). With the low consumption of N_2O at this temperature range, the N_2O concentration increases significantly. As the temperature increases, more of the hydrocarbon fuel has reacted and formed among other CO. This CO starts to react with N_2O, hence contributing to a decreasing growth in N_2O concentration. For cases 2 and 3, the reaction pathway surpasses the contribution by the formation pathways, leading to a decreasing trend in N_2O,

https://doi.org/10.1021/acs.energyfuels.3c02549
Energy Fuels XXXX, XXX, XXX−XXX

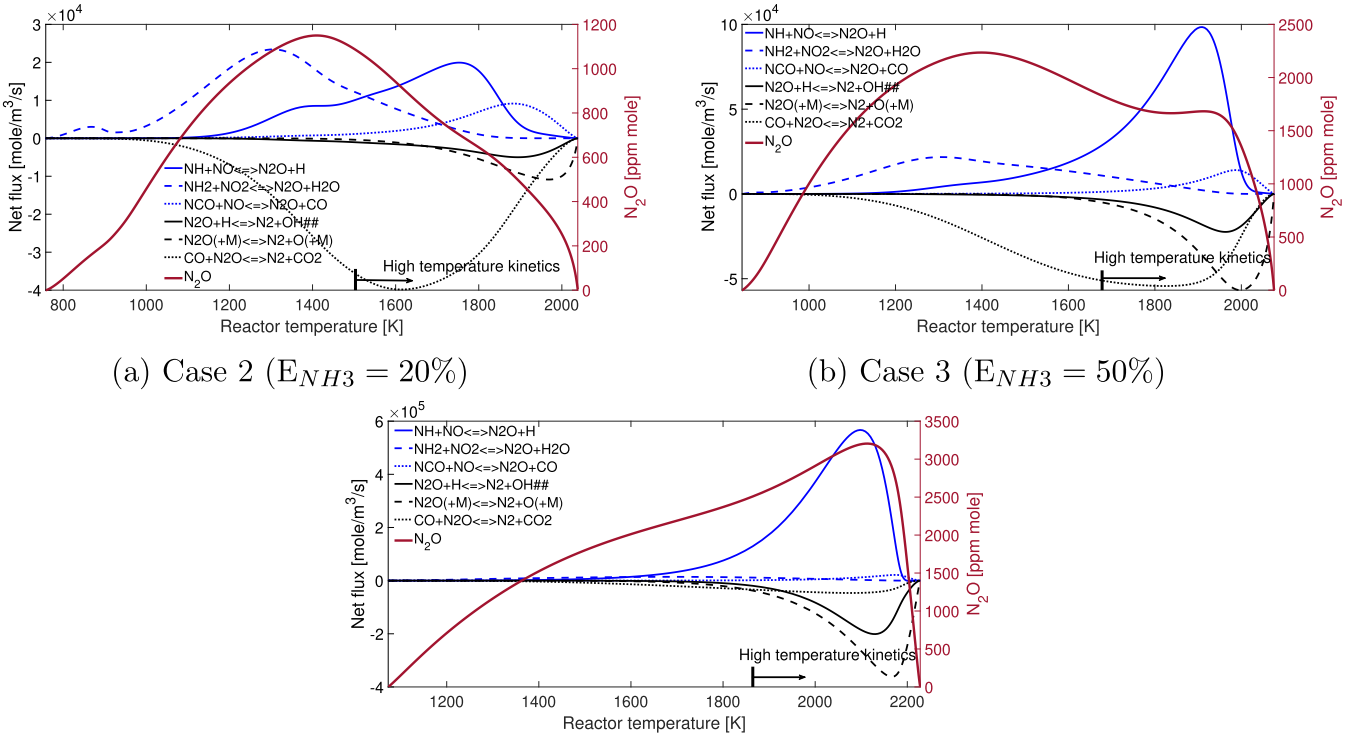

Figure 14. Three most producing and consuming reactions during ignition for cases 2−4, at ϕ = 0.6. Blue lines represent formation pathways. Black lines represent consuming pathways.

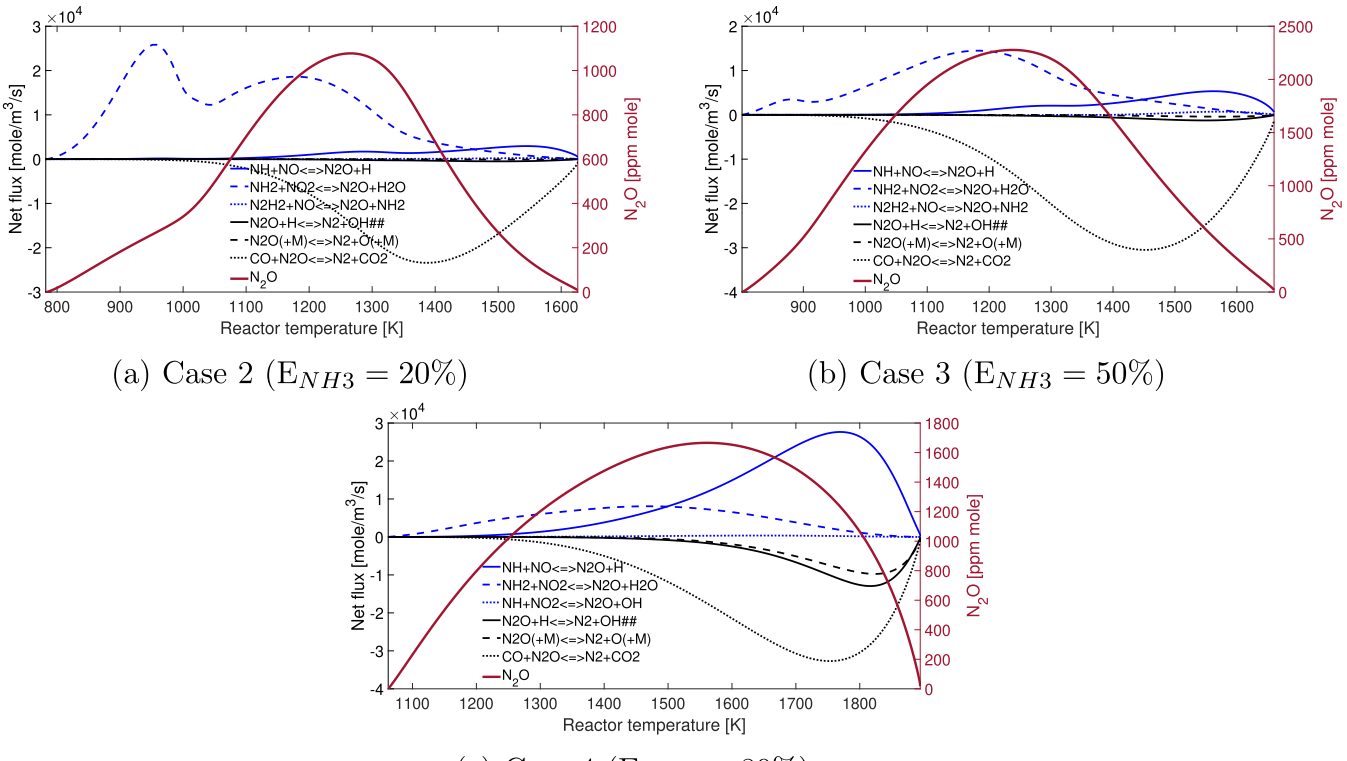

Figure 15. Three most producing and consuming reactions during ignition for cases 2−4, at ϕ = 3.6. Blue lines represent formation pathways. Black lines represent consuming pathways.

which can be seen in Figure 12. As more ammonia has reacted with other species, first to form NH_2, and then NH_2 reacts with OH and H to produce NH, the amount of NH has increased. This NH reacts with NO and quickly becomes the most

https://doi.org/10.1021/acs.energyfuels.3c02549
Energy Fuels XXXX, XXX, XXX−XXX

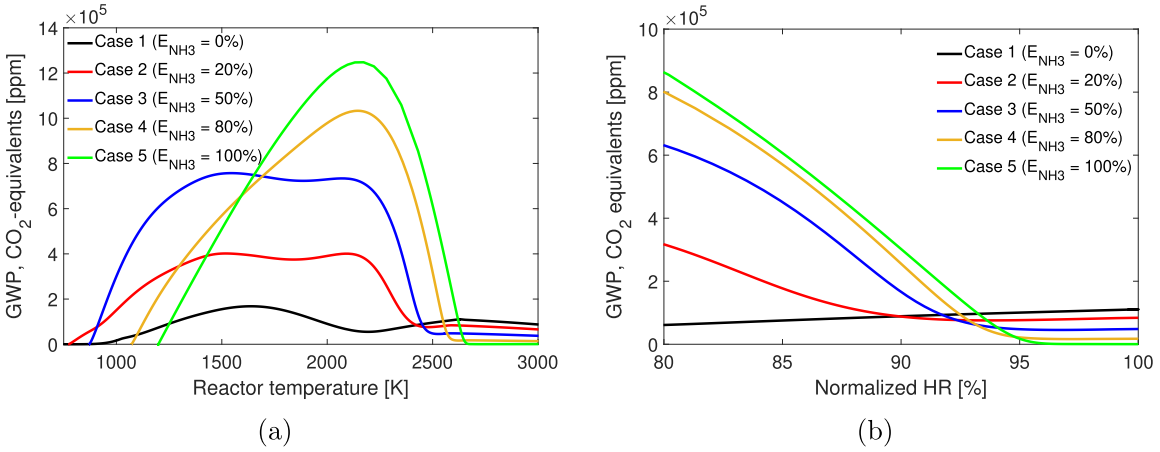

Figure 16. Global warming potential (GWP) during the ignition phase in the form of ppm of CO_2 equivalents ($X_{CO_2} + 298 \times X_{N_2O} + 25 \times X_{CH_4}$) vs reactor temperature (a)/energy released from the fuel (b) for an equivalence ratio of 1.0.

contributing reaction pathway for N_2O formation. At some point, this pathway's contribution increases above the consumption of the CO pathway, again creating an increasing N_2O concentration. The magnitude of the NH-consuming pathways is significantly higher than the NH_2-pathway; however, the consuming reactions increase accordingly in the relevant region.

The $CO + N_2O \rightleftharpoons N_2 + CO_2$ pathway keeps the N_2O concentrations low and is active through the whole ignition phase for all cases that include *n*-heptane. In case 4, the formation rate of N_2O is consistently higher than the consumption rate, until the single peak of N_2O is reached. However, the interaction with CO creates a less steep region. Notably, for cases including a sufficient amount of hydrocarbon fuel, interaction between NCO and NO leads to the formation of N_2O. Despite this, the sum of the contribution of the CO-consuming pathway and the NCO-formating pathway is negative, implying that the hydrocarbon fuel helps to keep the N_2O emissions down.

Toward the last 1/3 of the ignition period, the N_2O-consuming reactions become increasingly active, leading to a decreasing growth in N_2O and eventually consuming most of the produced N_2O. The reaction pathways mainly contributing to the consumption of N_2O are the abovementioned CO pathway $CO + N_2O \rightleftharpoons N_2 + CO_2$, by interaction with atomic hydrogen $N_2O + H \rightleftharpoons N_2 + OH$, and thermal dissociation to form nitrogen and an oxygen atom $[N_2O(+M) \rightleftharpoons N_2 + O(+M)]$. All the pathways mainly contribute toward the end of the ignition phase; however, it can be seen that the reducing pathway, including CO, is the main contributor at the lower temperatures, while the two last pathways mainly contribute in the high-temperature chemistry region.

In the case of pure *n*-heptane as a fuel, the level of formation of N_2O within the ignition phase is low (≈2 ppm) relative to the values obtained with ammonia. However, a peak is observed toward the end of the ignition phase, mainly produced by nitrogen reacting with oxygen and a third body. This obtained N_2O is consumed rather quickly by interaction with atomic hydrogen to form nitrogen and OH, offering low levels at the end of the ignition phase.

For rich and lean conditions, the temperatures obtained during the ignition period are significantly lower than those at stoichiometric conditions. This impacts the formation of N_2O during this phase. Figures 14 and 15 display the three-most N_2O-consuming and producing reaction pathways for cases 2, 3, and 4 at equivalence ratios of 0.6 (lean) and 3.6 (rich). The results show that the two main reactions leading to N_2O formation in this region are the same as those for stoichiometric conditions: NH reacting with NO and NH_2 reacting with NO_2. The consuming reactions are mainly by interactions between N_2O and CO, while toward higher temperatures and at higher ammonia concentrations, the interaction with H and a third body increases in influence. The $CO + N_2O \rightleftharpoons N_2 + CO_2$ pathway is observed to be the most dominant consuming reaction for both lean and rich conditions, as illustrated in Figures 14 and 15. Conversely, the $N_2O + H \rightleftharpoons N_2 + OH$ pathway is found to be the most consuming under stoichiometric conditions, as shown in Figure 12.

Compared to stoichiometric conditions, the influence of the $NH + NO \rightleftharpoons N_2O + H$ pathway is significantly lower during both lean and rich conditions. This is an impact of the lower temperatures during the ignition. This leads to the early formation of a single N_2O peak during the ignition period in cases 2 and 3, as N_2O mainly gets formed by interactions between NH_2 and NO_2, which, as discussed, is facilitated at lower temperatures. In case 4, one observes that the NH-containing reaction is superior to the NH_2 reaction, shifting the N_2O peak toward higher temperatures. Looking at the respective temperatures, one observes that as more ammonia is included in the fuel, the temperature range within the ignition period shifts to higher temperatures, a repercussion of the higher autoignition temperatures of ammonia. Figure 15 shows that case 4, under rich conditions, reaches temperatures above 1800 K, which could amplify those high-temperature reactions to be more active than those in the other two cases with lower ammonia concentrations.

4.4. Global Warming Potential. The impact of N_2O formation on the GWP is demonstrated for an equivalence ratio of 1.0 in Figure 16a,b. Figure 16a illustrates the GWP over the reactor temperatures, while Figure 16b portrays the GWP against the energy released from the fuel. The GWP is presented in CO_2 equivalents, calculated by summing the mole fraction of CO_2 with 298 times that of N_2O and 25 times that of methane based on their GWP on a 100 year horizon. The results show that during the ignition phase, the elevated N_2O concentrations caused by ammonia result in an offset in the climate benefits compared to when using pure *n*-heptane. However, as the combustion process progresses and reaches a fully burned state,

https://doi.org/10.1021/acs.energyfuels.3c02549
Energy Fuels XXXX, XXX, XXX−XXX

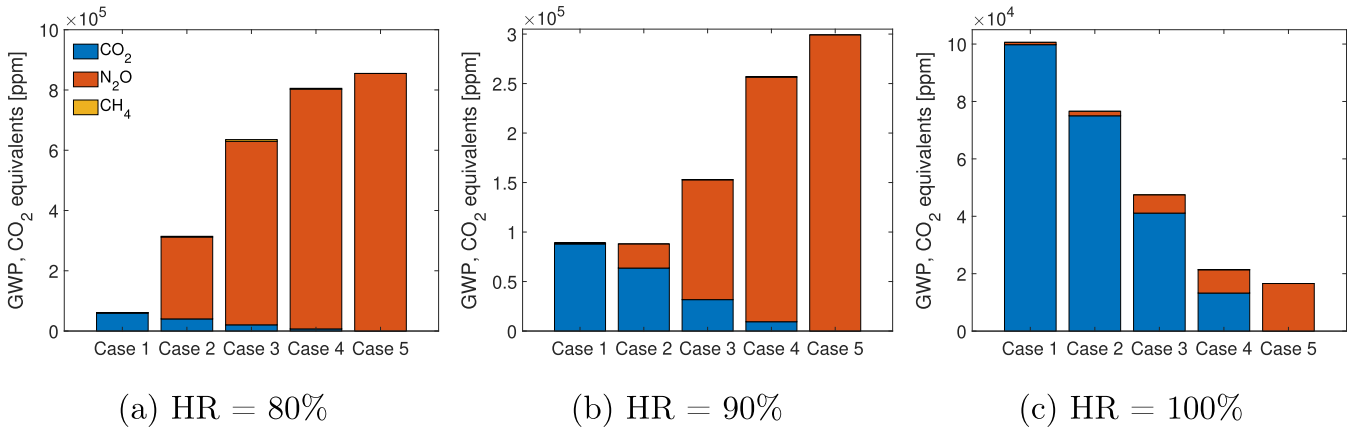

Figure 17. GWP at three different percentages of released fuel energy at an equivalence ratio of 1.0.

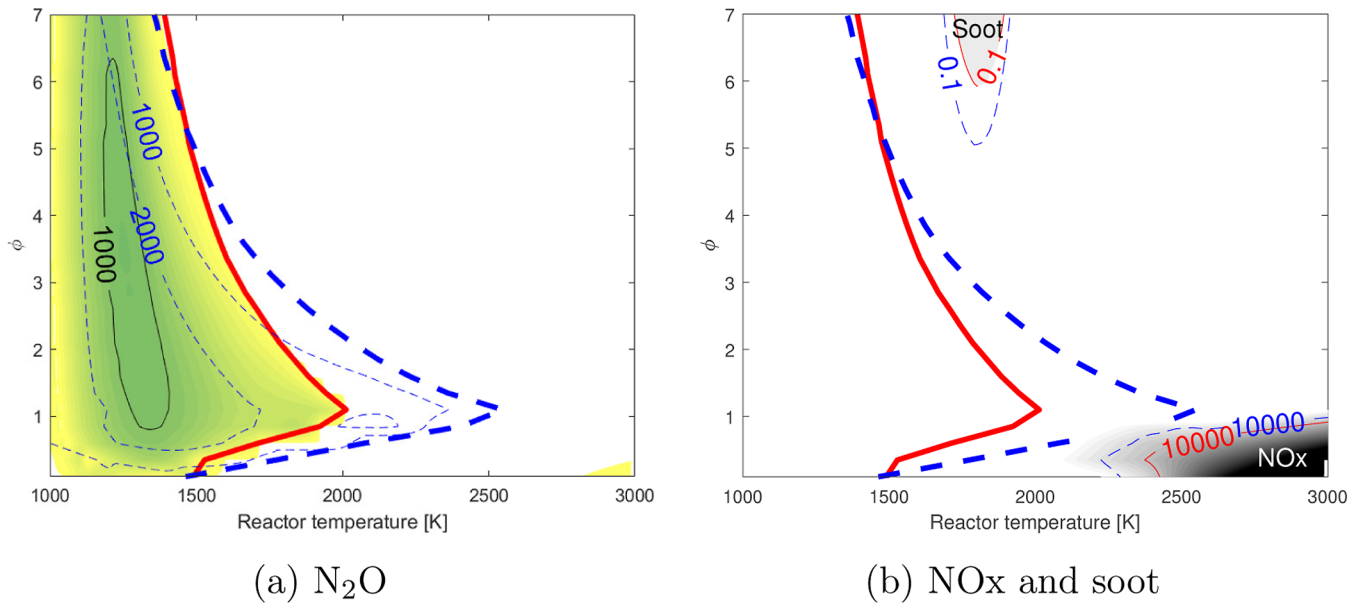

Figure 18. $\phi-T$ diagnostic map displaying NOx, Soot, and N_2O concentrations for diluted conditions (X_{O_2} = 10%) compared to air as an oxidizer for case 3. Blue dashed lines represent concentrations when air is the oxidizer.

the impact of N_2O on the CO_2-equivalents becomes negligible. Consequently, the GWP decreases with the amount of fuel-bound carbon under fully combusted conditions. Figure 16b reveals that to achieve GWP benefits in, for example, case 2, the fuel that has started to react must undergo substantial combustion with at least 90% of its energy to be released. For pure ammonia (case 5), approximately 93% of the energy from the fuel must be released. When more than 93% of the fuel energy is released at an equivalence ratio of 1.0, GWP advantages are achieved in all the cases that include ammonia. It is observed that for lower and higher equivalence ratios, a higher energy conversion is needed to achieve favorable GWP compared to *n*-heptane operation.

Figure 17 identifies which of the species, N_2O, CO_2, and CH_4, is responsible for the GWP at three different energy conversion states. When 80% of the fuel energy is released, the offset in GWP for cases that include ammonia is caused by N_2O. CO_2 concentrations are the primary contributor to GWP for *n*-heptane, whereas decreases in influence with higher AES. At 90% energy release, the influence of N_2O decreases, although, compared to pure *n*-heptane, it causes significantly elevated GWP in cases with an AES higher than 50%. When all fuel energy is released, corresponding to a fully burned state, CO_2 becomes the most significant contributor to GWP in all cases with *n*-heptane, resulting in a monotonic decrease in GWP with AES.

The simulations in this study apply to conditions where a reaction in the zero-dimensional homogeneous reactor is initiated and evolves in time according to chemical kinetics. It is important to note that the energy release in these simulations does not perfectly represent the combustion efficiency found in the actual engines. In real engines, mixture inhomogeneities may cause incomplete combustion and unburned fuel. This can explain why lower levels of N_2O are achieved in experimental engine studies compared to this work.

4.5. Effects of Dilution. The effect of diluting the oxidizer for case 3 is shown in Figure 18a,b. Here, the oxidizer consists of 10% oxygen and 90% nitrogen. Figure 18a shows the N_2O concentrations for case 3 with the oxidizer diluted and the isocontours of regular air operation. The figure shows that by dilution, the resulting N_2O concentrations can be significantly lower, just exceeding 1000 ppm, while regular operation exceeds

https://doi.org/10.1021/acs.energyfuels.3c02549
Energy Fuels XXXX, XXX, XXX−XXX

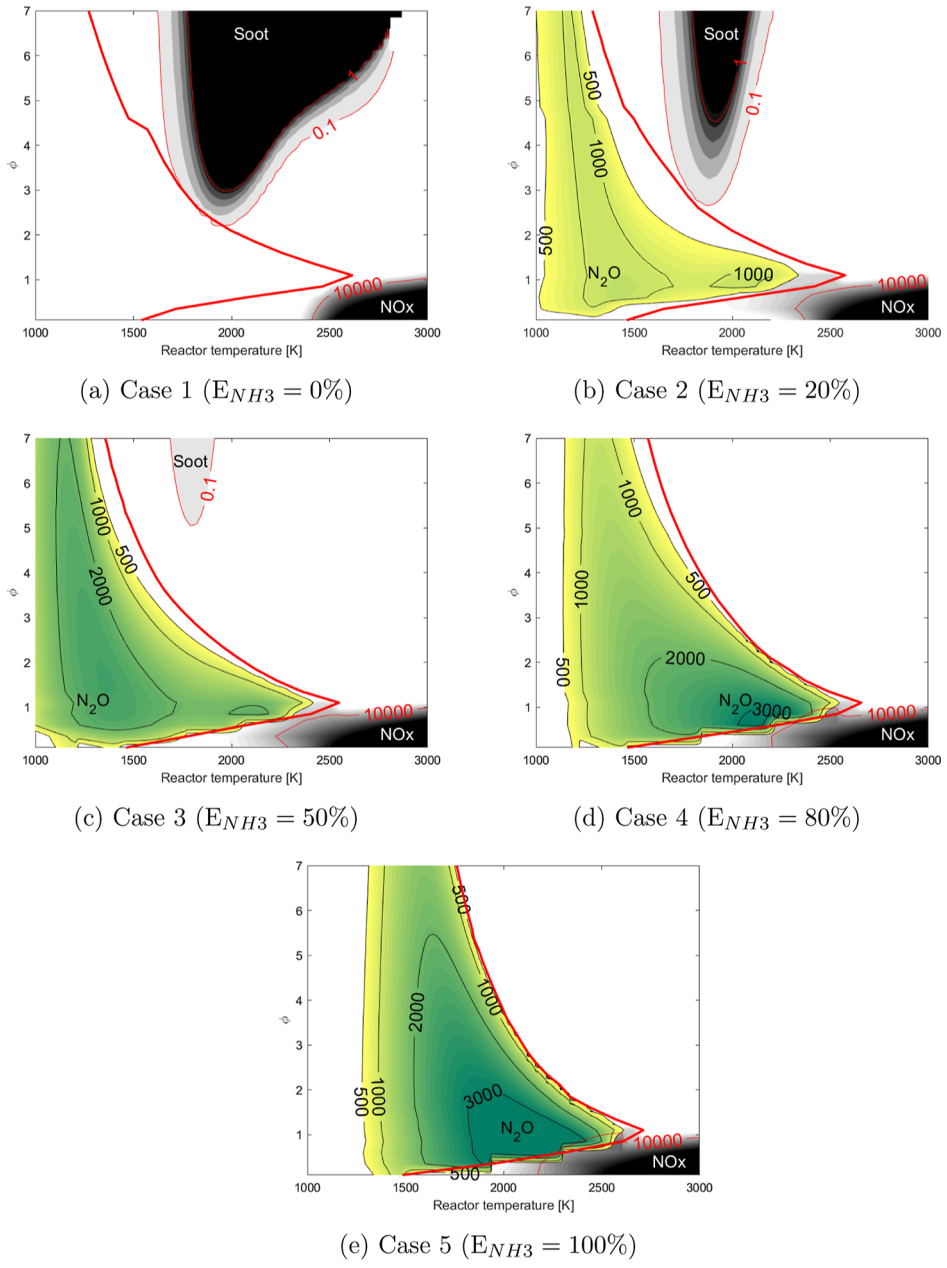

Figure 19. $\phi-T$ diagnostic map for the five fuel blends.

2000 ppm. Figure 18b shows that the soot formation region shifts to slightly higher equivalence ratios compared with air as the oxidizer. The high-level NO_x area is located under similar conditions; however, a shift to higher temperatures is observed. The most prominent change by applying dilution is related to the N_2O region.

The leading cause of change in N_2O emissions is the lower temperature increase during combustion, an effect of dilution. As most N_2O is formed during the ignition (see Section 4.3), the N_2O region becomes narrower under diluted conditions. The reduction in temperature rise leads to a considerable decrease (by 1−2 orders of magnitude) in the contribution of several pathways, particularly the NH + NO ⇌ N_2O + H reaction that is associated with high-temperature chemistry. Additionally, the reduced difference between the consuming reactions (primarily CO + N_2O ⇌ N_2 + CO_2) and the producing pathways helps maintain lower concentrations compared to air operation. Further details on the reaction pathways during dilution can be found in the Supporting Information S.B.

Since LTC strategies typically operate in diluted conditions, complete combustion could be obtained at lower temperatures. This indicates that LTC strategies could yield low N_2O emissions. Moreover, exhaust gas recirculation (EGR) is an often-applicable method for LTC strategies. In addition to a lower temperature increase during combustion, applying EGR introduces the mixture to more C atoms bound in exhaust species. This could lead to even further reduced N_2O concentrations, as one could assume that the reducing pathway through interaction between N_2O and CO, as discussed in Section 4.3, could increase in influence.

Akihama et al.[41] observed that the soot formation region was slightly narrower and tended toward higher equivalence rations when an EGR of 50% was applied for their hydrocarbon fuel. Although they defined the EGR as a mixture of CO_2, H_2O, and

https://doi.org/10.1021/acs.energyfuels.3c02549
Energy Fuels XXXX, XXX, XXX−XXX

N_2, a comparable trend is observed in the present study when diluting the oxidizer by increasing the diluent N_2.

The shift to higher temperatures for the NO_x and lower temperatures for the N_2O region creates a broader area without high emissions. Dilution entails fully combusted conditions obtained at lower temperatures. However, this could decrease the availability of oxygen. Lower oxygen content may inhibit ammonia burnout and overall lead to increased N_2O emissions in realistic conditions. When interpreting the $\phi-T$ maps, these effects should be considered. Further research should be performed regarding dilution, including the possible increased N_2O consumption through CO. However, the argument of fully combusted conditions to yield low N_2O emissions also holds for diluted conditions.

4.6. Diagnostic Maps. In this section, the resulting $\phi-T$ maps from Sections 4.1 and 4.2 are combined and presented in Figure 19a−e. Here, the limits for visibility for each of the three emissions are set as follows: For NO_x, concentrations above 5000 ppm are included and shaded to show variations up to 20,000 ppm. For the soot, the lower limit is set to 0.1%, while the distinguishable upper limit is 1%. Lastly, the boundaries for N_2O are set to show concentrations between 500 and 3000 ppm. In addition, isocontours are set to mark the 10,000 ppm limit for NO_x, 0.1 and 1% limits for soot, and 500, 1000, 2000, and 3000 ppm limits for N_2O. Similar to the previous results, a thick red line distinguishes the ignition phase and equilibrium results.

The five $\phi-T$ maps in Figure 19 highlight the influence of how altering the fuel composition can affect the potential for emissions formation. All three pollutants addressed in this work exhibit changes when changing the fuel composition. The exception for substantial changes is the NO_x levels above 10,000 ppm, which are located at high temperatures and low equivalence ratios for all cases. The soot yield region is apparent only in cases 1, 2, and 3. For cases 4 and 5, the potential for soot is below the set limit in this work and, generally, very low (Section 4.2). Considerations for rich conditions for cases 1 and 2 are important as the soot region for these fuel compositions stretches to relatively low equivalence ratios. For case 3, the soot region is located in the upper middle part of the map, with only the 0.1% limit visible. When half of the energy contribution in the fuel comes from ammonia, the soot presence is considerably reduced, but nitrogen-related emissions are of more significant concern. Analyzing the diagnostic maps, one can conclude that, in general, the favorable injection strategies for avoiding thermal NO_x formation (region embraced by the 10,000 ppm limit) shall remain similar as in pure diesel, i.e., avoiding high temperatures. However, in cases with ammonia bypassing operation at high temperatures, it is not enough since still substantial levels of NO_x can be created via the fuel nitrogen route. Thus, higher equivalence ratios at medium to high temperatures seem to be preferable. Although, the majority of fuel NO is created during the ignition process creating an emission island corresponding to the N_2O region, yet at lean conditions emerging beyond the ignition line to merge with the thermal NO_x island. Thus, optimal injection strategies reaching equilibrium at lower temperatures thanks to dilution, as shown in Section 4.5 should be considered.

Kitamura et al.[42] presented a $\phi-T$ map, including injection strategies to avoid high-emission regions. The expected conditions for HCCI, low-temperature-rich combustion, and modulated kinetics (MK) combustion strategies were displayed. These are all low-temperature combustion strategies that aim to achieve sufficiently premixed conditions between the fuel and oxidizer in a globally diluted environment, allowing combustion to occur at lower temperatures. This could potentially create conditions coinciding with the N_2O region. However, the importance of the diluted approach should be considered, as shown in Section 4.5. This investigation revealed that emissions are affected if the fuel mixture experiences local conditions different from global conditions.

Interpreting the results with high N_2O emissions occurring during the ignition shows that it is essential to ensure fully combusted conditions to achieve low N_2O emissions. As presented in the introduction, operating strategies play a crucial role and should be addressed accordingly. When it comes to controlling the addressed emissions, an increase in the AES appears to be favored by fuel-rich conditions. Nevertheless, it is important to consider that emissions, such as HCN or unburned ammonia, could increase under such conditions.

5. SUMMARY AND CONCLUSIONS

The effect on NO_x, N_2O, and soot emissions by including ammonia in a dual-fuel diesel engine was addressed in this work. Equivalence ratio−temperature diagrams were created for five different fuels, including ammonia and *n*-heptane (0/100, 20/80, 50/50, 80/20, and 100/0 energy-share of NH_3/*n*-C_7H_{16}), highlighting regions with expected NO_x, N_2O, and soot emissions. CPR simulations created the diagrams for an extensive range of initial conditions. A new method for obtaining results was suggested, dividing the maps into two different regions: one region with elevated equilibrium temperatures after 2 ms and one region with transient results during the ignition. The following conclusions can be drawn from this study:

- N_2O concentrations are elevated during the ignition, and the magnitude of the concentrations increases with the AES, going from single-digit ppm levels for pure *n*-heptane to above 3000 ppm by moles for pure ammonia. The increased concentrations are related to the formation through species originating from ammonia decomposition. Specifically, NH_2 at lower temperatures and NH at higher temperatures.
- Under fully combusted conditions, the N_2O emissions remain generally low and fuel-independent. These concentrations align with the thermal NO conditions traced to the splitting of NO.
- Carbon in the fuel prevents the accumulation of N_2O by the pathway $CO + N_2O \rightleftharpoons N_2 + CO_2$ during most of the ignition phase. Toward the end of the ignition phase, production of N_2O through NCO ($NCO + NO \rightleftharpoons N_2O + CO$) increases; however, it does not surpass the consumption through CO. Together with the low-temperature chemistry accompanying the hydrocarbon fuel, the suppressing of N_2O leads to two N_2O peaks for cases with high *n*-heptane content in the fuel mixture.
- Elevated N_2O concentration during ignition offsets the GWP when ammonia is included in the fuel. As a result, at least 90% of the fuel energy must be released to achieve GWP benefits when including ammonia in the fuel. Under fully combusted conditions, the GWP decreases with increasing AES.
- NO_x concentrations depend on the fuel composition, displaying a nonlinear behavior with AES during the ignition phase. The highest concentrations during the ignition are observed for 20% of AES and decrease with higher or lower shares. The behavior is a consequence of

https://doi.org/10.1021/acs.energyfuels.3c02549
Energy Fuels XXXX, XXX, XXX−XXX

varying contributions from fuel NO, prompt NO, and the thermal De-NO_x mechanism. Emissions surpassing 10,000 ppm, however, are fuel-independent and determined by the thermal NO mechanism.

- The potential for soot formation is highly dependent on the share of hydrocarbons in the fuel and is considerable in rich conditions when the ammonia share is below 50%. While the introduction of ammonia in the fuel reduces and moves the potential for soot formation to higher equivalence ratios, it introduces a potential for other emissions, such as hydrogen cyanide and unburned ammonia.
- Oxidizer dilution is shown to be beneficial in diminishing the N_2O region by achieving equilibrium at lower temperatures. The lower temperatures directly affect the formation of N_2O through high-temperature reactions, in particular, NH + NO ⇌ N_2O + H. This creates a region on the $\phi-T$ diagrams with low concentrations of soot, NO_x, and N_2O emissions, showing a promising effect of the implementation of duel-fuel ammonia combustion within LTC strategies.

The performed chemical kinetic study revealed several dominating N_2O formation and reduction pathways depending on temperature, equivalence ratio, fuel composition, and dilution. The risk of having N_2O emissions can be greatly minimized by assuring complete ammonia combustion, as this work suggests that the increased N_2O formation observed with increased ammonia content is related to the ignition and burnout of the fuel. Therefore, preventing interruption of the combustion (i.e., flame quenching on the walls) could inhibit increased GHG potential. Further, burning ammonia rich seems to be favorable to producing low NO_x and N_2O emissions. However, the potential for other drawbacks, i. e., ammonia slip,[9] is an issue at higher equivalence ratios. Based on these findings, future studies are necessary to identify physical locations and occurrences of the phenomena mentioned above using CFD supported by experimentally validated emissions data.

■ ASSOCIATED CONTENT

Supporting Information

The Supporting Information is available free of charge at https://pubs.acs.org/doi/10.1021/acs.energyfuels.3c02549.

$\phi-T$ diagrams for the method applying constant temperature and pressure; reaction pathways for N_2O formation under dilution; HCN concentrations for cases 1 to 4 on $\phi-T$ diagrams (PDF)

■ AUTHOR INFORMATION

Corresponding Author

Krister A. Pedersen − *Department of Energy and Process Engineering, NTNU Norwegian University of Science and Technology, NO-7491 Trondheim, Norway;* orcid.org/0009-0009-2854-4257; Email: krister.a.pedersen@ntnu.no

Authors

Michał T. Lewandowski − *Department of Energy and Process Engineering, NTNU Norwegian University of Science and Technology, NO-7491 Trondheim, Norway;* orcid.org/0000-0002-9990-6552

Corinna Schulze-Netzer − *Department of Energy and Process Engineering, NTNU Norwegian University of Science and Technology, NO-7491 Trondheim, Norway;* orcid.org/0000-0002-4445-7243

Michał Pasternak − *LOGE Polska Sp. z o.o., 42-200 Częstochowa, Poland*

Terese Løvås − *Department of Energy and Process Engineering, NTNU Norwegian University of Science and Technology, NO-7491 Trondheim, Norway*

Complete contact information is available at: https://pubs.acs.org/10.1021/acs.energyfuels.3c02549

Author Contributions

Krister A. Pedersen: investigation, methodology, software, validation, formal analysis, and writing—original draft. Michał T. Lewandowski: conceptualization, investigation, methodology, and writing—review and editing. Corinna Schulze-Netzer: software, analysis, and writing—review and editing. Michał Pasternak: software and writing—review and editing. Terese Løvås: writing—review and editing, supervision, project administration, and funding acquisition.

Notes

The authors declare no competing financial interest.

■ ACKNOWLEDGMENTS

The authors acknowledge financial support from the Norwegian Research Council and the National Centre for Research and Development in Poland through the Norway and Poland grants (contract no. NOR/POLNOR/ACTIVATE/0046/2019-00) for the ACTIVATE project "Ammonia as carbon-free fuel for internal combustion engine driven agricultural vehicle" (https://ammoniaengine.org). Financial support is also acknowledged to the Nordic Energy Research (NER) and the Norwegian Research Council through the CAHEMA project within the Nordic Maritime Transport and Energy Research Programme. The authors thank Valentin Scharl for the discussion on the original $\phi-T$ map creation.

■ REFERENCES

(1) IEA. *Global Energy Review 2021*; IEA: Paris, 2021.

(2) IEA. *Greenhouse Gas Emissions from Energy: Overview*, 2021. https://www.iea.org/reports/greenhouse-gas-emissions-from-energy-overview.

(3) Mertens, J.; Belmans, R.; Webber, M. Why the Carbon-Neutral Energy Transition Will Imply the Use of Lots of Carbon. *C* **2020**, *6*, 39.

(4) Al-Baghdadi, M. An Overview of Hydrogen as an Alternative Fuel. *Encyclopedia*, 2020; Vol. *6*, pp 1−22.

(5) Verhelst, S.; Wallner, T. Hydrogen-fueled internal combustion engines. *Prog. Energy Combust. Sci.* **2009**, *35*, 490−527.

(6) Ishimoto, Y.; Voldsund, M.; Nekså, P.; Roussanaly, S.; Berstad, D.; Gardarsdottir, S. O. Large-scale production and transport of hydrogen from Norway to Europe and Japan: Value chain analysis and comparison of liquid hydrogen and ammonia as energy carriers. *Int. J. Hydrogen Energy* **2020**, *45*, 32865−32883.

(7) Gray, D. S.; Domke, C. J.; Meguerian, G. H.; Mieville, R. L. *Ammonia Application to Reciprocating Engines Volume 2, Report No. 1054*; Continental Aviation And Engineering Corp Detroit MI: Detroit, MI, USA, 1967.

(8) Han, D.; Liu, Y.; Huang, Z. *Engines and Fuels for Future Transport*; Kalghatgi, G., Agarwal, A. K., Leach, F., Senecal, K., Eds.; Springer Singapore: Singapore, 2022; pp 233−256.

(9) Reiter, A. J.; Kong, S.-C. Combustion and emissions characteristics of compression-ignition engine using dual ammonia-diesel fuel. *Fuel* **2011**, *90*, 87−97.

(10) Wolfram, P.; Kyle, P.; Zhang, X.; Gkantonas, S.; Smith, S. Using ammonia as a shipping fuel could disturb the nitrogen cycle. *Nat. Energy* **2022**, *7*, 1112−1114.

(11) Myhre, G.; Shindell, D.; Bréon, F.-M.; Collins, W.; Fuglestvedt, J.; Huang, J.; Koch, D.; Lamarque, J.-F. D.; Lee, B. M.; Nakajima, T.; Robock, A.; Stephens, G.; Takemura, T.; Zhang, H. Anthropogenic and Natural Radiative Forcing. *Climate Change 2013—The Physical Science Basis: Working Group I Contribution to the Fifth Assessment Report of the Intergovernmental Panel on Climate Change*; Stocker, T. F., Qin, D., Plattner, G.-K., Tignor, M., Allen, S. K., Boschung, J., Nauels, A., Xia, Y., Bex, V.; Midgley, P. M., Eds.; Cambridge University Press: Cambridge, United Kingdom and New York, NY, USA, 2014; pp 659−740.
(12) Prather, M. J.; Hsu, J.; DeLuca, N. M.; Jackman, C. H.; Oman, L. D.; Douglass, A. R.; Fleming, E. L.; Strahan, S. E.; Steenrod, S. D.; Søvde, O. A.; Isaksen, I. S. A.; Froidevaux, L.; Funke, B. Measuring and modeling the lifetime of nitrous oxide including its variability. *J. Geophys. Res.* **2015**, *120*, 5693−5705.
(13) Glarborg, P. The $NH_3/NO_2/O_2$ system: Constraining key steps in ammonia ignition and N_2O formation. *Combust. Flame* **2023**, *257*, 112311.
(14) Yousefi, A.; Guo, H.; Dev, S.; Liko, B.; Lafrance, S. Effects of ammonia energy fraction and diesel injection timing on combustion and emissions of an ammonia/diesel dual-fuel engine. *Fuel* **2022**, *314*, 122723.
(15) Gross, C. W.; Kong, S.-C. Performance characteristics of a compression-ignition engine using direct-injection ammonia−DME mixtures. *Fuel* **2013**, *103*, 1069−1079.
(16) Ramalingam, S.; Rajendran, S.; Ganesan, P.; Govindasamy, M. Effect of operating parameters and antioxidant additives with biodiesels to improve the performance and reducing the emissions in a compression ignition engine—A review. *Renewable Sustainable Energy Rev.* **2018**, *81*, 775−788.
(17) Zhou, X.; Li, T.; Wang, N.; Wang, X.; Chen, R.; Li, S. Pilot diesel-ignited ammonia dual fuel low-speed marine engines: A comparative analysis of ammonia premixed and high-pressure spray combustion modes with CFD simulation. *Renewable Sustainable Energy Rev.* **2023**, *173*, 113108.
(18) Nadimi, E.; Przybyla, G.; Lewandowski, M. T.; Adamczyk, W. Effects of ammonia on combustion, emissions, and performance of the ammonia/diesel dual-fuel compression ignition engine. *J. Energy Inst.* **2023**, *107*, 101158.
(19) Wu, X.; Feng, Y.; Gao, Y.; Xia, C.; Zhu, Y.; Shreka, M.; Ming, P. Numerical simulation of lean premixed combustion characteristics and emissions of natural gas-ammonia dual-fuel marine engine with the pre-chamber ignition system. *Fuel* **2023**, *343*, 127990.
(20) Niki, Y.; Nitta, Y.; Sekiguchi, H.; Hirata, K. Diesel Fuel Multiple Injection Effects on Emission Characteristics of Diesel Engine Mixed Ammonia Gas Into Intake Air. *J. Eng. Gas Turbines Power* **2019**, *141*, 061020.
(21) Li, H.; Neill, W. S.; Guo, H.; Chippior, W. The NOx and N2O Emission Characteristics of an HCCI Engine Operated With n-Heptane. *J. Energy Resour. Technol.* **2011**, *134*, 011101.
(22) Zhang, M.; Xu, W.; Wang, R.; Wei, X.; Wang, J.; Huang, Z.; Tan, H. Wall heat loss effect on the emission characteristics of ammonia swirling flames in a model gas turbine combustor. *Combust. Flame* **2023**, *256*, 112955.
(23) Hayakawa, A.; Hayashi, M.; Kovaleva, M.; Gotama, G. J.; Okafor, E. C.; Colson, S.; Mashruk, S.; Valera-Medina, A.; Kudo, T.; Kobayashi, H. Experimental and numerical study of product gas and N2O emission characteristics of ammonia/hydrogen/air premixed laminar flames stabilized in a stagnation flow. *Proc. Combust. Inst.* **2023**, *39*, 1625−1633.
(24) Okafor, E. C.; Somarathne, K. A.; Ratthanan, R.; Hayakawa, A.; Kudo, T.; Kurata, O.; Iki, N.; Tsujimura, T.; Furutani, H.; Kobayashi, H. Control of NOx and other emissions in micro gas turbine combustors fuelled with mixtures of methane and ammonia. *Combust. Flame* **2020**, *211*, 406−416.
(25) Tang, R.; Xu, Q.; Pan, J.; Gao, J.; Wang, Z.; Wei, H.; Shu, G. An experimental and modeling study of ammonia oxidation in a jet stirred reactor. *Combust. Flame* **2022**, *240*, 112007.
(26) Glarborg, P.; Miller, J. A.; Ruscic, B.; Klippenstein, S. J. Modeling nitrogen chemistry in combustion. *Prog. Energy Combust. Sci.* **2018**, *67*, 31−68.
(27) Ariemma, G. B.; Sorrentino, G.; Ragucci, R.; de Joannon, M.; Sabia, P. Ammonia/Methane combustion: Stability and NOx emissions. *Combust. Flame* **2022**, *241*, 112071.
(28) Ariemma, G. B.; Sorrentino, G.; Sabia, P.; Ragucci, R.; de Joannon, M. MILD Combustion of Methanol, Ethanol and 1-Butanol binary blends with Ammonia. *Proc. Combust. Inst.* **2023**, *39*, 4509−4517.
(29) Zhou, M.; Yan, F.; Ma, L.; Jiang, P.; Wang, Y.; Ho Chung, S. Chemical speciation and soot measurements in laminar counterflow diffusion flames of ethylene and ammonia mixtures. *Fuel* **2022**, *308*, 122003.
(30) Zhang, K.; Xu, Y.; Li, Y.; Liu, Y.; Wang, B.; Wang, H.; Ma, J.; Cheng, X. Effects of ammonia on morphological characteristics and nanostructure of soot in the combustion of diesel surrogate fuels. *J. Hazard. Mater.* **2023**, *445*, 130645.
(31) Shao, C.; Campuzano, F.; Zhai, Y.; Wang, H.; Zhang, W.; Mani Sarathy, S. Effects of ammonia addition on soot formation in ethylene laminar premixed flames. *Combust. Flame* **2022**, *235*, 111698.
(32) Li, Y.; Zhang, Y.; Yang, G.; Fuentes, A.; Han, D.; Huang, Z.; Lin, H. A comparative study on PAH characteristics of ethanol and ammonia as fuel additives in a premixed flame. *J. Energy Inst.* **2022**, *101*, 56−66.
(33) Li, Y.; Zhang, Y.; Zhan, R.; Huang, Z.; Lin, H. Experimental and kinetic modeling study of ammonia addition on PAH characteristics in premixed n-heptane flames. *Fuel Process. Technol.* **2021**, *214*, 106682.
(34) (a) Xu, Y.; Mao, Q.; Wang, Y.; Luo, K. H.; Zhou, L.; Wang, Z.; Wei, H. Role of ammonia addition on polycyclic aromatic hydrocarbon growth: A ReaxFF molecular dynamics study. *Combustion and Flame* **2023**, *250*, 112651. (b) Xu, L.; Chang, Y.; Treacy, M.; Zhou, Y.; Jia, M.; Bai, X.-S. A skeletal chemical kinetic mechanism for ammonia/n-heptane combustion. *Fuel* **2023**, *331*, 125830.
(35) Zaher, M. H.; Yousefi, A.; Dadsetan, M.; Liko, B.; Lafrance, S.; Guo, H.; Thomson, M. J. Characterization of soot emissions formed in a compression ignition engine cofired by ammonia and diesel. *Fuel* **2023**, *349*, 128715.
(36) Kane, S. P.; Northrop, W. F. Thermochemical Recuperation to Enable Efficient Ammonia-Diesel Dual-Fuel Combustion in a Compression Ignition Engine. *Energies* **2021**, *14*, 7540.
(37) Lewandowski, M. T.; Pasternak, M.; Haugsvær, M.; Løvås, T. Simulations of ammonia spray evaporation, cooling, mixture formation and combustion in a direct injection compression ignition engine. *Int. J. Hydrogen Energy* **2023**.
(38) Scharl, V.; Sattelmayer, T. Ignition and combustion characteristics of diesel piloted ammonia injections. *Fuel Commun.* **2022**, *11*, 100068.
(39) Ryu, K.; Zacharakis-Jutz, G. E.; Kong, S.-C. Performance characteristics of compression-ignition engine using high concentration of ammonia mixed with dimethyl ether. *Appl. Energy* **2014**, *113*, 488−499.
(40) Ichikawa, Y.; Niki, Y.; Takasaki, K.; Kobayashi, H.; Miyanagi, A. NH3 combustion using three-layer stratified fuel injection for a large two-stroke marine engine: Experimental verification of the concept. *Appl. Energy Combust. Sci.* **2022**, *10*, 100071.
(41) Akihama, K.; Takatori, Y.; Inagaki, K.; Sasaki, S.; Dean, A. M. Mechanism of the smokeless rich diesel combustion by reducing temperature. *SAE Trans.* **2001**, *110*, 648−662.
(42) Kitamura, T.; Ito, T.; Senda, J.; Fujimoto, H. Mechanism of smokeless diesel combustion with oxygenated fuels based on the dependence of the equivalence ratio and temperature on soot particle formation. *Int. J. Engine Res.* **2002**, *3*, 223−248.
(43) Wenming, Y.; Meng, Y. Phi-T map analysis on RCCI engine fueled by methanol and biodiesel. *Energy* **2019**, *187*, 115958.
(44) Lewandowski, M. T.; Netzer, C.; Emberson, D. R.; Løvås, T. Numerical investigation of glycerol/diesel emulsion combustion in compression ignition conditions using Stochastic Reactor Model. *Fuel* **2022**, *310*, 122246.

https://doi.org/10.1021/acs.energyfuels.3c02549
Energy Fuels XXXX, XXX, XXX−XXX

(45) Hasan, M. M.; Rahman, M. M. Homogeneous charge compression ignition combustion: Advantages over compression ignition combustion, challenges and solutions. *Renewable Sustainable Energy Rev.* **2016**, *57*, 282−291.
(46) An, Y.; Jaasim, M.; Vallinayagam, R.; Vedharaj, S.; Im, H. G.; Johansson, B. Numerical simulation of combustion and soot under partially premixed combustion of low-octane gasoline. *Fuel* **2018**, *211*, 420−431.
(47) Cao, L.; Bhave, A.; Su, H.; Mosbach, S.; Kraft, M.; Dris, A.; McDavid, R. M. Influence of Injection Timing and Piston Bowl Geometry on PCCI Combustion and Emissions. *SAE Int. J. Engines* **2009**, *2*, 1019−1033.
(48) Shrestha, K. P.; Seidel, L.; Zeuch, T.; Moréac, G.; Dagaut, P.; Mauss, F. On the implications of nitromethane − NO chemistry interactions for combustion processes. *Fuel* **2021**, *289*, 119861.
(49) Zhu, D.; Qu, Z.; Li, M.; Agarwal, S.; Fernandes, R.; Shu, B. Investigation on the NO formation of ammonia oxidation in a shock tube applying tunable diode laser absorption spectroscopy. *Combust. Flame* **2022**, *246*, 112389.
(50) Seidel, L.; Moshammer, K.; Wang, X.; Zeuch, T.; Kohse-Höinghaus, K.; Mauss, F. Comprehensive kinetic modeling and experimental study of a fuel-rich, premixed n-heptane flame. *Combust. Flame* **2015**, *162*, 2045−2058.
(51) Mauß, F. Entwicklung eines kinetischen Modells der Rußbildung mit schneller Polymerisation. Ph.D. Thesis, Göttingen: Cuvillier, 1998.
(52) Shrestha, K. P.; Seidel, L.; Zeuch, T.; Mauss, F. Detailed Kinetic Mechanism for the Oxidation of Ammonia Including the Formation and Reduction of Nitrogen Oxides. *Energy Fuels* **2018**, *32*, 10202−10217.
(53) Shrestha, K. P.; Vin, N.; Herbinet, O.; Seidel, L.; Battin-Leclerc, F.; Zeuch, T.; Mauss, F. Insights into nitromethane combustion from detailed kinetic modeling − Pyrolysis experiments in jet-stirred and flow reactors. *Fuel* **2020**, *261*, 116349.
(54) Yin, G.; Xiao, B.; Zhan, H.; Hu, E.; Huang, Z. Chemical kinetic study of ammonia with propane on combustion control and NO formation. *Combust. Flame* **2023**, *249*, 112617.
(55) Pan, J.; Tang, R.; Wang, Z.; Gao, J.; Xu, Q.; Shu, G.; Wei, H. An experimental and modeling study on the oxidation of ammonia and n-heptane with JSR. *Proc. Combust. Inst.* **2023**, *39*, 477−485.
(56) *LOGEresearch v1.10*; LOGE AB, 2018.
(57) Thorsen, L. S.; Jensen, M. S.; Pullich, M. S.; Christensen, J. M.; Hashemi, H.; Glarborg, P.; Alekseev, V. A.; Nilsson, E. J.; Wang, Z.; Mei, B.; Liu, N.; Ju, Y. High pressure oxidation of NH3/n-heptane mixtures. *Combust. Flame* **2023**, *254*, 112785.
(58) Wang, B.; Dong, S.; Jiang, Z.; Gao, W.; Wang, Z.; Li, J.; Yang, C.; Wang, Z.; Cheng, X. Development of a reduced chemical mechanism for ammonia/n-heptane blends. *Fuel* **2023**, *338*, 127358.

NOTE ADDED AFTER ASAP PUBLICATION

This paper was published ASAP on October 27, 2023. An additional citation was added to reference 34, and the corrected version was reposted on October 30, 2023.

https://doi.org/10.1021/acs.energyfuels.3c02549
Energy Fuels XXXX, XXX, XXX−XXX